

## INFORMATION TO USERS

This manuscript has been reproduced from the microfilm master. UMI films the text directly from the original or copy submitted. Thus, some thesis and dissertation copies are in typewriter face, while others may be from any type of computer printer.

**The quality of this reproduction is dependent upon the quality of the copy submitted.** Broken or indistinct print, colored or poor quality illustrations and photographs, print bleedthrough, substandard margins, and improper alignment can adversely affect reproduction.

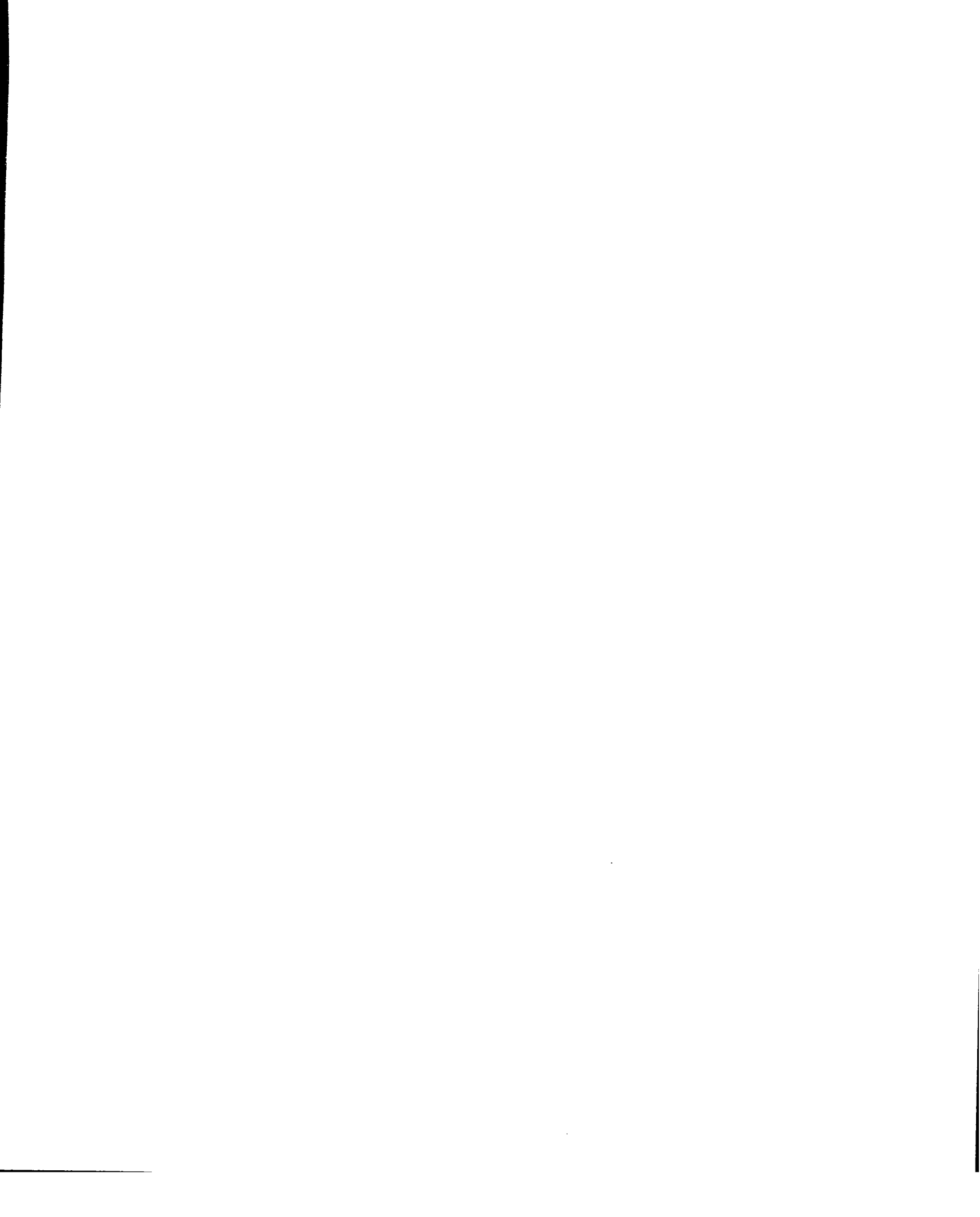
In the unlikely event that the author did not send UMI a complete manuscript and there are missing pages, these will be noted. Also, if unauthorized copyright material had to be removed, a note will indicate the deletion.

Oversize materials (e.g., maps, drawings, charts) are reproduced by sectioning the original, beginning at the upper left-hand corner and continuing from left to right in equal sections with small overlaps.

Photographs included in the original manuscript have been reproduced xerographically in this copy. Higher quality 6" x 9" black and white photographic prints are available for any photographs or illustrations appearing in this copy for an additional charge. Contact UMI directly to order.

ProQuest Information and Learning  
300 North Zeeb Road, Ann Arbor, MI 48106-1346 USA  
800-521-0600

**UMI<sup>®</sup>**



UNIVERSITY OF OKLAHOMA  
GRADUATE COLLEGE

DETERMINING THE DISTANCE OF SN 1987A WITH SEAM

A Dissertation SUBMITTED TO THE GRADUATE FACULTY  
In Partial Fulfillment of the Requirements for the Degree of

Doctor of Philosophy

ROBERT C. MITCHELL

Norman, Oklahoma

2001

UMI Number: 3023442

**UMI<sup>®</sup>**

---

UMI Microform 3023442

Copyright 2001 by Bell & Howell Information and Learning Company.

All rights reserved. This microform edition is protected against  
unauthorized copying under Title 17, United States Code.

---

Bell & Howell Information and Learning Company  
300 North Zeeb Road  
P.O. Box 1346  
Ann Arbor, MI 48106-1346

Copyright © 2001, by ROBERT C. MITCHELL

All rights reserved.

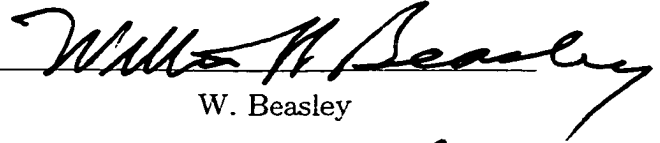
DETERMINING THE DISTANCE OF SN 1987A WITH SEAM

A Dissertation APPROVED FOR THE  
DEPARTMENT OF PHYSICS AND ASTRONOMY

BY



E. Baron (Chair)



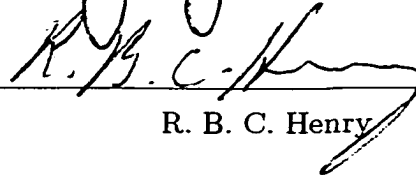
W. Beasley



D. Branch



J. J. Cowan



R. B. C. Henry

# Contents

<b>1</b>	<b>Distance Scale</b>	<b>1</b>
1.1	Standard Candles . . . . .	1
1.2	Cosmological Core-Collapse . . . . .	1
1.3	SEAM . . . . .	2
1.4	Outline . . . . .	3
<b>2</b>	<b>Models</b>	<b>5</b>
2.1	PHOENIX . . . . .	5
2.2	Rezoning . . . . .	6
2.3	Other Problems . . . . .	7
<b>3</b>	<b>Days 1-14</b>	<b>10</b>
3.1	Weak Balmer Lines . . . . .	10
3.2	Nickel Mixing . . . . .	11
3.3	More Evidence for Nickel Mixing . . . . .	13
3.4	Days 1-2 . . . . .	15
3.5	Days 3-4 . . . . .	15
3.6	Days 8-14 . . . . .	16
<b>4</b>	<b>Days 18-103</b>	<b>30</b>
4.1	Temperature Profile . . . . .	30
4.2	Days 18-24 . . . . .	32
4.3	Days 30-81 . . . . .	33
4.4	Day 103 . . . . .	33
<b>5</b>	<b>Distance Measurement</b>	<b>46</b>
5.1	The PHOENIX Distance . . . . .	46
5.2	Other Distances . . . . .	47
<b>6</b>	<b>Conclusions</b>	<b>54</b>
6.1	Results . . . . .	54
6.2	Further Research . . . . .	55

**7 Appendix** **60**  
7.1 REZONE..... 60

# List of Tables

2.1	Days of Blinnikov Models . . . . .	9
3.1	Photospheric Temperature . . . . .	18
3.2	Best-Fit Nickel Mass Fractions . . . . .	19
4.1	Required Changes in Luminosities . . . . .	35
5.1	Models, Best-fit Luminosities . . . . .	49
5.2	Observed Photometry . . . . .	50
5.3	Moduli . . . . .	51
5.4	Least-squares Fits of Color Moduli Graph . . . . .	52
5.5	Other Distance Calculations . . . . .	53

# List of Figures

3.1	Gamma-ray energy deposition vs. $\tau$ for Day 4.52, Blinnikov et al.'s model, with and without nickel (Blinnikov 1999; Blinnikov et al. 2000). . . . .	17
3.2	PHOENIX model spectrum for Day 1.36. . . . .	20
3.3	PHOENIX model spectrum for Day 2.67. . . . .	21
3.4	PHOENIX model spectrum for Day 3.59. . . . .	22
3.5	PHOENIX model spectrum for Day 4.52, without additional nickel mixing. . . . .	23
3.6	PHOENIX model spectrum for Day 4.52, with gamma-ray deposition calculated assuming local deposition due to a constant nickel mass fraction of $1.0 \times 10^{-3}$ everywhere in the envelope. 75-layer model. . . . .	24
3.7	PHOENIX model spectrum for Day 8.37, without additional nickel mixing. . . . .	25
3.8	PHOENIX model spectrum for Day 8.37, with a nickel mass fraction of $1.0 \times 10^{-4}$ everywhere in the envelope, and a tapp value of $1.0 \times 10^{-3}$ . . . . .	26
3.9	PHOENIX model spectrum for Day 10.12, without additional nickel mixing. . . . .	27
3.10	PHOENIX model spectrum for Day 10.12, with a nickel mass fraction of $1.0 \times 10^{-3}$ everywhere in the envelope, and a tapp value of $1.0 \times 10^{-3}$ . . . . .	28
3.11	PHOENIX model spectrum for Day 14.52, with a nickel mass fraction of $1.0 \times 10^{-4}$ everywhere in the envelope, and a tapp value of $1.0 \times 10^{-3}$ . 75-layer model. . . . .	29
4.1	Probability of best-fit vs. relative increase in luminosity from model's base value, according to FITS.PRO. . . . .	34
4.2	PHOENIX model spectrum for Day 18.70, with an increase in luminosity of 21.3% from Blinnikov's original value. No additional nickel mixing. . . . .	36
4.3	PHOENIX model spectrum for Day 24.38, with an increase in luminosity of 34.7% from Blinnikov's original value. No additional nickel mixing. . . . .	37
4.4	PHOENIX model spectrum for Day 30.90, with an increase in luminosity of 36.0% from Blinnikov's original value. No additional nickel mixing. . . . .	38
4.5	PHOENIX model optical spectrum for Day 58.62, with Blinnikov's original luminosity value. No additional nickel mixing. . . . .	39
4.6	PHOENIX model UV spectrum for Day 58.62, with Blinnikov's original luminosity value. No additional nickel mixing. . . . .	40

4.7	PHOENIX model optical spectrum for Day 58.62 with an increase in luminosity of 28.0% from Blinnikov's original value. No additional nickel mixing. . . . .	41
4.8	PHOENIX model UV spectrum for Day 58.62, with an increase in luminosity of 28.0% from Blinnikov's original value. No additional nickel mixing. . . . .	42
4.9	PHOENIX model optical spectrum for Day 81.35, with an increase in luminosity of 8.7% from Blinnikov's original value. No additional nickel mixing. . . . .	43
4.10	PHOENIX model UV spectrum for Day 81.35, with an increase in luminosity of 8.7% from Blinnikov's original value. No additional nickel mixing. . . . .	44
4.11	PHOENIX model spectrum for Day 103.68, with Blinnikov's original luminosity and no additional nickel mixing. . . . .	45
5.1	Color moduli derived for 1987A. Solid line: least-squares fit for all data. Dashed line: least-squares fit excluding Days 18 and 24. Dot-dashed line: least-squares fit excluding Days 18 and 24 and all UV data. . . . .	52

## **Abstract**

Supernovae count among the most luminous phenomena in the universe, and as such they have been sought after to serve as cosmological distance indicators. Type Ia supernovae are currently the most commonly used indicators. In this study, we will examine a method for using Type II supernovae as distance indicators, and attempt to prove this method's reliability and accuracy by calculating the distance to the Type II Supernova 1987A and comparing it to results using other methods.

# Chapter 1

## Distance Scale

### 1.1 Standard Candles

Distance determinations are at the heart of observational cosmology. Type Ia supernovae are most often chosen as distance indicators because of their theoretically uniform characteristics. All type Ia's are believed to originate from the explosion of white dwarfs near the Chandrasekhar mass limit, and therefore would have similar luminosity curves. Other types (Ib, Ic, and II, the core-collapse supernovae) originate from the explosion of any star above  $8 M_{\odot}$  and hence can have much more varied luminosities, making it much more difficult to obtain an accurate distance modulus.

### 1.2 Cosmological Core-Collapse

As of the preparation of this thesis, the farthest type Ia supernova yet detected was at a redshift of  $z = 1.7$  (Riess et al. 2001), which places the time of detonation at least 11 billion years ago, into the era when the universe was decelerating. We hope to be able to see many more supernovae at these look-back times and further back in the near

future.

White dwarfs originate from stars of less than  $8 M_{\odot}$ , hence they rarely take less than a billion years to form, and most will be well below the Chandrasekhar mass limit. To reach the mass required for sudden detonation, they must usually accumulate matter from a nearby companion star, and this accumulation is likely to be interrupted or even prevented by frequent nova outbursts. Even the steadiest and fastest accumulation could take up to another billion years or so before reaching the mass limit. The type Ia seen at  $z = 1.7$  may well have been one of the first Ia's in the history of the Universe, and therefore we may be unlikely to see large numbers of Ia's even further back in time.

Core-collapse supernovae, which originate from high-mass stars, can take as little as a few million years to occur. We should therefore be able to detect these supernovae as far back as the formation of the very first stars, estimated to be around  $z = 5$ . In order to get as complete a picture as possible about the history of the Universe's expansion, we cannot become dependent on the type Ia distance scale, and so it becomes imperative that we develop alternate means of measuring cosmological distances.

### 1.3 SEAM

The Spectral-Fitting Expanding Atmosphere Method (SEAM) can be used to calculate the distance to supernovae or other stellar objects for which luminosities cannot be easily predicted (see Baron et al. 1995, and references therein). Computer models of the radiative and hydrodynamic structure of such an object are used to create a synthetic spectrum and calculate the subsequent luminosity. This spectrum is compared with an observed spectrum, and if they match, one calculates the color luminosities predicted by the model and compares them to observed color magnitudes. A series of distance moduli  $\mu$  can therefore be determined. Practical application of this method on supernovae,

however, has been limited by the availability and quality of spectroscopic and bolometric observations, and by the limitations of hydrodynamic models.

In this study, I will demonstrate that the radiative transfer code PHOENIX can be used to examine the radiation-hydro models of Type II supernovae, make corrections for discrepancies in their prediction of spectral evolution, and successfully calculate the distance to the supernovae with unparalleled accuracy. My test subject is Supernova 1987A, the most well-observed and well-studied supernova to date.

My work here utilized the hydrodynamic model 14E1 developed by Nomoto and collaborators and modelled using the STELLA software package (Blinnikov 1999; Blinnikov et al. 2000). This model calculated the light curve for up to six months after the explosion, and includes allowance for time-dependent, multi-group radiation hydrodynamics, monochromatic scattering effects, and the effects of spectral lines on the opacity.

## 1.4 Outline

The procedure for synthesizing the spectral evolution of SN 1987A from Blinnikov et al.'s model is described in Chapter 2. Chapter 3 details the results from Day 1 to Day 14 as calculated by PHOENIX, and compares them to the observed evolution. During this period, it quickly becomes evident that a substantial mixing of nickel into the envelope is required for the model spectra to match the observed spectra. Chapter 4 continues the spectral evolution through Day 103. This is the period during which the Blinnikov models produce spectra that are too bright or too dim in parts of their spectrum. Usually, the red portion of the visible is too bright in the synthetic spectrum, although in the case of Day 103 the synthetic spectrum is too blue. In Chapter 5, I will take the luminosities of all the best-fit spectral models and use them to calculate the distance to SN 1987A, then compare my results with other distance estimates. Chapter 6 will

summarize the work I have done here and my plans for future work. Appendix A contains descriptions of subsidiary codes developed during the course of my research.

In the illustrations of the observed vs. model spectra of SN 1987A which are used in this paper, all optical spectra are taken from the archive of Cerro-Tololo observatory (CTIO) (Phillips et al. 1988). All UV spectra are from the International Ultraviolet Explorer (IUE) (Pun et al. 1995). Wherever possible, important lines are identified.

## Chapter 2

# Models

### 2.1 PHOENIX

PHOENIX is a general radiation transfer code that computes temperature, opacity, and level populations for each of a specified number of radial zones in a moving stellar envelope. PHOENIX allows the user to calculate level populations for a multitude of different nuclear species in LTE or non-LTE (Hauschildt and Baron 1999; Short et al. 1999). The following is a list of the species which were calculated in NLTE for this study: H I, He I, He II, C I, O I, Ne I, Na I, Mg II, Si II, S II, Ca I, Ca II, Ti II, Fe I, Fe II, Fe III, and Co II.

The Blinnikov et al. hydrodynamic model consists of an ejecta envelope divided into 300 zones, with compositions defined for each layer (Blinnikov 1999; Blinnikov et al. 2000). The outer layers of this model were re-zoned onto the grid that is used by PHOENIX, preserving the compositions in velocity-space. The inner boundary condition was taken to be diffusive, which is well justified in these calculations. The gamma-ray deposition function, which is the energy in gamma-rays absorbed by the atoms in the envelope per unit mass per unit time, is calculated for each new zone. The new grid was

chosen so as to maintain both composition and density profiles with adequate resolution.

At the onset of this research project, all available versions of PHOENIX utilized a 50-zone grid. As work progressed, it eventually became clear that increased resolution was necessary in order to successfully converge the models for all but the earliest days. Therefore, the PHOENIX program package was modified to use a 75-zone model, after which convergence of latter-day models was possible. Subsequently increasing the number of zones to 100, and switching from a serial version of PHOENIX to parallel, has further improved the results. All PHOENIX spectra illustrated in this paper are from 100-layer models unless otherwise noted.

The days since explosion for which Blinnikov hydrodynamic models were used are listed in Table 2.1, along with Julian Date equivalents.

## 2.2 Rezoning

Model resolution is dependent on there being no large jumps in parameter values from one zone to the next (a good rule of thumb is that there should be a minimum span of three zones per decade range of temperatures, opacities, etc.). Severe discontinuities in zone parameters make it difficult or even impossible for the model to converge and the numerical results are inaccurate. Good resolution is especially required at a model's photosphere and/or ionization front, and the ionization front can move in space as the model converges to radiative equilibrium.

To alleviate this problem, it became necessary to adjust the zone boundaries to create thinner zones where they were needed to increase resolution. I have created the program REZONE to accomplish this. REZONE rewrites the PHOENIX layer file to insert a new zone boundary within a pre-selected, pre-existing zone, and at the same time removes a pre-selected zone boundary from where it is not needed, so as to maintain

the set number of zones.

## 2.3 Other Problems

In many cases, iterations of a particular model have to be halted when temperature inversions begin to emerge. The temperature profile of a supernova envelope generally should have a steadily decreasing (or flat) temperature with increasing radius, but in an inversion the temperature begins increasing with increasing radius during model iterations. The result is that radiation from a particular layer will be transported inward instead of outward, and the effects upon PHOENIX models are almost always deleterious and the model fails to converge. To correct a temperature inversion, one can manually edit the temperature values in the model for each affected layer. If this is not practical, another recourse is to abandon the model at this point and restart at an earlier iteration with corrections that will hopefully prevent the temperature inversion from reappearing.

Still another method is to activate a parameter called "tapp" in PHOENIX that forces an isothermal temperature profile for the outermost layers (which is close to the converged solution for low optical depths). "tapp" is set equal to an optical depth below which the model is kept isothermal. This makes the models somewhat more difficult to converge, since the temperature changes after each iteration no longer occur naturally, but it prevents the temperatures of the outermost layers from exploding and is also helpful for controlling temperature inversions, thereby preventing program crashes.

There is another parameter in PHOENIX called "accit," which is the number of accelerated lambda iterations the program performs to solve the radiative transfer problem.

The accelerated lambda iterations are performed on the matrix equations:

$$J = \Lambda S[J],$$

$$J_{new} = \Lambda^* S_{new} + (\Lambda - \Lambda^*) S_{old},$$

where  $J$  is the mean intensity and  $S$  is the source function which depends on the value of  $J$  (the subscript indicates which  $J$  is used in the source function.  $\Lambda$  is the full lambda operator and  $\Lambda^*$  is a judiciously chosen approximate lambda operator (Hauschildt and Baron 1999). Machine accuracy is required for complete convergence. The default value of `accit` is 50 iterations, with the option of increasing to 200 if the supernova model is in its nebular phase. It was found that even some early-time models (e.g. Day 4) would not converge in `accit` within 50 iterations. As a result it may be impossible to converge the model, however machine accuracy while desirable is not always required, particularly if the model converges to radiative equilibrium. It became necessary to reset `accit` in PHOENIX to 200 iterations for all cases. While this generally will increase the program's run time, it can have the advantage of making the temperature values easier to converge, which will in turn reduce the run time.

Table 2.1: Days of Blinnikov Models

day <sup>1</sup>	JD <sup>2</sup> 2446800+	date (UT)
1.364	51.255	24.755 Feb
2.665	52.556	26.056 Feb
3.592	53.483	26.983 Feb
4.524	54.415	27.915 Feb
8.374	58.265	3.765 Mar
10.115	60.006	5.506 Mar
14.519	64.410	9.910 Mar
18.839	68.730	14.230 Mar
24.378	74.269	19.769 Mar
30.896	80.787	26.287 Mar
58.619	108.510	23.010 Apr
81.354	131.245	15.745 May
103.68	153.57	7.07 Jun

<sup>1</sup>Days since shock breakout, which occurred roughly 0.075 days after explosion (personal communication, S. I. Blinnikov).

<sup>2</sup>Based upon neutrino burst detection at Kamiokande II and IMB, JD 2446849.816 (23.316 Feb 1987; 07.35 UT). (Hirata et al. 1987; Bionta et al. 1987; Phillips et al. 1988)

# Chapter 3

## Days 1-14

### 3.1 Weak Balmer Lines

Referring to Figures 3.2 and 3.3, one sees that the PHOENIX spectra for Days 1 and 2 are in extremely good agreement with the observed spectra, to within a small fraction of a magnitude. At Day 3, however, there begins to be a discrepancy between the strengths of the observed Balmer lines and the calculated Balmer lines. This discrepancy worsens as we advance in the time-evolution to Day 14, by which time the predicted lines are barely visible.

Schmutz et al. (1990), using various hydrodynamic models, noted the hydrogen atoms appeared to be sufficiently excited to create strong lines, despite the fact that the photospheric temperature had dropped below the ionization threshold ( $T \approx 6000K$ ). They could offer no explanation for this discrepancy. The pure H/He non-LTE model of Takeda (1991) also resulted in weak Balmer lines, as did a model by Hauschildt and Ensman (1994), which used an earlier version of PHOENIX with H I, He I, Mg II, and Ca II in NLTE and metal line blanketing in LTE. These two groups suggested that differences between the theoretical and actual density distributions might be responsible.

In theory, a lower photosphere temperature would cause a corresponding drop in electron density due to a lack of sufficient hydrogen ionization, resulting in weaker hydrogen lines. Table 3.1 shows the general decrease in the calculated photosphere temperature vs. the corresponding PHOENIX model day. The temperature listed for each day is that for the layer in the model for which  $\tau_{\text{std}}$  is closest to the value of 1, assuming that the line-forming region lies in this vicinity. ( $\tau_{\text{std}} \equiv$  total continuum optical depth at 5000 Å). For Days 1 and 2, the gas temperature is well above the ionization threshold for hydrogen and thus can maintain the required electron density. From Day 3 onward, this is no longer the case, therefore some other agent must be responsible for maintaining an electron density sufficient to produce strong Balmer lines.

Current models of SN 87A have a lower H abundance and higher He abundance than solar values. The first theory was to use solar abundances in the model (i.e. more H and less He), hoping it would provide more free electrons and thus strengthen the Balmer lines. The results were negative. The next theory, involving radioactive  $^{56}\text{Ni}$  produced better results. Figure 3.1 shows the gamma-ray deposition function predicted by Blinnikov et al.'s hydrodynamic model for Day 4. The function determines the probability that an atom in the model envelope will absorb and be ionized by a gamma-ray photon from  $^{56}\text{Ni}$ . The figure clearly shows that the deposition is negligible for all but the innermost layers of the model ( $\tau_{\text{std}} > 100$ ), and is therefore insufficient to excite the hydrogen atoms.

## 3.2 Nickel Mixing

In order for the synthetic Balmer lines to match the strength of the observed lines, it is necessary to either increase the temperature of the model or increase the gamma-ray deposition. The latter would require mixing into the supernova's outer envelope a greater

amount of  $^{56}\text{Ni}$  than exists in Blinnikov et al.'s model (Blinnikov 1999; Blinnikov et al. 2000). In PHOENIX this can be accomplished by replacing the self-consistent deposition function from the Blinnikov et al. model with an ad hoc function that simulates a gamma-ray population created by excess nickel mixing, assuming a uniform mass fraction of  $^{56}\text{Ni}$  distributed homogeneously and complete local deposition of gamma-rays. The new deposition function is therefore much more uniform than the original (see figure 3.1), allowing for more hydrogen ionization and excitation in the line-forming region while at the same time preventing saturation of the innermost layers.

Comparisons between the synthetic spectrum and the actual spectrum provide a sensitive probe for how much  $^{56}\text{Ni}$  must be mixed into the supernova envelope. Although the model produced by PHOENIX utilized a constant distribution, this by no means precludes the possibility of inhomogeneous mixing. It serves only to indicate that a minimum quantity of nickel must be mixed further out into the envelope than previous models suggest, in order to generate the extra gamma rays necessary to ionize the hydrogen.

It will be seen that nickel mixing continues to play an important role at least through Day 14. Table 3.2 shows the nickel mass fraction values that my PHOENIX models have required to produce best-fit synthetic spectra for Days 3–14, as well as values of  $\tau_{\text{app}}$ , where applicable. Note that the value required to produce lines of the proper strength begins to decrease after Day 4. By this time, it can no longer be considered a good approximation to assume complete local deposition of gamma-rays, due to the decreasing density of the supernova envelope in the line-forming region. Since the nickel mass fraction in PHOENIX is a representation of the amount of absorbed  $^{56}\text{Ni}$  gamma-rays, a lower value indicates the decreasing number of gamma-rays that are actually being absorbed due to the increasing transparency of the envelope.

### 3.3 More Evidence for Nickel Mixing

The mechanism for the mixing of  $^{56}\text{Ni}$  into the envelope is the subject of intense debate, and won't be settled until the core-collapse supernova mechanism is better understood. Kifonidis et al. (2000) and Kifonidis et al. (in press) suggested that nickel mixing into the hydrogen shell would be suppressed in Type II supernovae due to strong deceleration at the He/H boundary. Nevertheless, evidence exists to support the results of the PHOENIX models. Early detection of X-rays (Dotani et al. 1987) and gamma-rays (Matz et al. 1988), the expansion velocities in infrared line widths (Erickson et al. 1988; Witteborn et al. 1989) and in  $^{56}\text{Co}$  gamma-ray lines (Barthelmy et al. 1989), the detection of H velocities as low as  $800 \text{ km s}^{-1}$  at Day 221 (Höflich 1988), and the late detection of the He I 10830 line (Fassia and Meikle 1999) suggest that significant mixing has occurred in the ejecta (see references in Arnett et al. 1989; McCray 1993).

Two-dimensional, axially symmetric models calculated by Fryxell et al. (1991) and by Herant and Benz (1991, 1992) suggested that  $^{56}\text{Ni}$  could be mixed into the envelope via finger-like structures that are produced shortly after the explosion by instabilities in the matter behind the shock front. By  $t = 90$  days, these fingers of nickel had broken up and expanded through radioactive heating into low-density bubbles of cobalt or iron, the decay products of  $^{56}\text{Ni}$ .

Inhomogeneous mixing has already been suggested as an explanation for the so-called "Bochum event," an emission satellite on the red side of the  $\text{H}\alpha$  line in Days 20–100. Utrobin et al. (1995) theorized that a high-velocity clump of  $^{56}\text{Ni}$  caused an asymmetric over-excitation of hydrogen in the outer envelope. Recent studies by the Chandra observatory have detected the presence of diffuse high-velocity Fe bubbles at the outer edge of the Cassiopeia A supernova remnant. Hughes et al. (2000) noted the detection of Fe bubbles at the outer edge of the supernova ejecta, outside the Si-

rich layers, and suggested that their diffuse nature could be explained by radioactive heating from decaying nickel. Since PHOENIX can simulate homogeneous mixing only, the Bochum event should not appear in the PHOENIX models, and referring to the best-fit synthetic spectra of this period shows that this is indeed the case.

Models of the composition of 87A in the nebular phase by Kozma and Fransson (1998a), based on the results of various explosion models [see references therein], used a number fraction of iron of  $2 \times 10^{-5}$  in the hydrogen layer, with a filling factor  $f \approx 0.17$ – $0.70$ . This corresponds to a mass fraction on the order of  $10^{-3}$ . The results of their simulations (Kozma and Fransson 1998b) indicated that the iron mass fraction should be within a factor of 2 of the predicted value. Li et al. (1993) theorized that the light curve of 87A during the nebular phase was dominated by  $\approx 0.078 M_{\odot}$  of  $^{56}\text{Co}$  in the form of 50–100 clumps. Their models contained nickel clumps that were initially opaque to gamma rays with  $f < 0.01$ , accounting for  $\approx 1\%$  of the total envelope mass. Gamma-ray absorption heated the clumps, causing them to expand until  $f = 0.5$ . The nickel mass fraction and total mass values predicted by the PHOENIX runs are well within the limits imposed by these two studies.

Detection of the He I 10830 line at times after 10 days suggests that helium is also being reionized by  $^{56}\text{Ni}$  decay. Fassia and Meikle (1999) applied spectral synthesis models to 87A and noted that the best fit to the helium line required at least 3% of the total  $^{56}\text{Ni}$  mass ( $0.07 M_{\odot}$ ) be mixed to above  $3000 \text{ km s}^{-1}$ , but that  $^{56}\text{Ni}$  concentrations should be negligible above  $\approx 4000 \text{ km s}^{-1}$ . Fassia and collaborators had previously done a similar analysis of the Type II supernova 1995V (Fassia et al. 1998), where they noted the best fit to the He line required the  $^{56}\text{Ni}$  density to be constant up to  $650$ – $1150 \text{ km s}^{-1}$ , then fall off by a power law of 8–9. Only  $10^{-6} M_{\odot}$  of  $^{56}\text{Ni}$  was required above the helium photosphere ( $\approx 4250 \text{ km s}^{-1}$  at Day 69) in 95V models. Burrows and Riper (1995), using Monte Carlo calculations of gamma-ray transport in clumpy debris

models of 87A's envelope, suggests that up to 50% of the total  $^{56}\text{Ni}$  mass in 87A should remain below  $1000 \text{ km s}^{-1}$ .

Herant et al. (1994) suggest that significant iron/nickel inversion may be the result of neutrino-driven convection within the fraction of a second just prior to the supernova explosion. Convection would destroy the spherical symmetry of the elemental distribution, possibly creating the iron/nickel clumps predicted and/or detected in later stages. This theory is supported by 2D hydrodynamic simulations performed by Kifonidis et al. (in press), although in their models the nickel was strongly decelerated at the He/H interface.

### 3.4 Days 1-2

Figure 3.2 and 3.3 plot the model graphs of Day 1.36 and Day 2.67 against observed optical and UV spectra. The most important optical lines visible are  $\text{H}\alpha$  through  $\text{H}\delta$ . In Day 1, He I  $\lambda 5876$  is also observed, although by Day 2 this line has virtually disappeared and the Ca II H&K doublet is beginning to emerge. No observed optical spectrum for Day 2 (Feb 26) was available (Phillips et al. 1988).

### 3.5 Days 3-4

By Day 3.59, the Ca II lines have become stronger, and there is now much greater line blanketing in the UV. Note that the predicted  $\text{H}\alpha$  line is now noticeably weaker than the observed line, a discrepancy that increases at Day 4.52. Note also that by Day 4 the Balmer lines in Blinnikov's model are slightly redshifted, because the observed lines formed at a higher velocity.

Figure 3.6 shows the results of modeling the Day 4 spectrum with constant gamma-ray deposition, resulting from a nickel mass fraction of  $1.0 \times 10^{-3}$  in the envelope.

The fit between the predicted lines and the actual lines is much better, illustrating the validity of this model. Assuming complete deposition, which is an acceptable approximation given the densities of the envelope this early in its evolution, a mass fraction of  $1.0 \times 10^{-3}$  corresponds to a requirement of approximately  $(1.0\text{--}1.2) \times 10^{-5} M_{\odot}$  of nickel to distribute enough gamma rays above the line forming region of the envelope.

It is evident from the Day 4 model that, while mixing nickel into the outer layers of the ejecta improves the fit in the optical, it significantly increases the error in the UV fit. This indicates that our assumption of homogeneous mixing fails, since the UV spectrum is formed at higher layers than the optical spectrum, and the UV fit is much better without nickel.

### **3.6 Days 8-14**

From Day 8.37 to Day 14.52, the synthetic Balmer lines are almost nonexistent without nickel mixing. It is observed that models in this period with nickel mass fractions slightly lower than what was required would produce  $H\alpha$  lines that were the correct strength but were slightly redshifted with respect to the observed lines. This indicates that excess nickel is required not only to produce the desired strength but to ensure the line forms at the correct velocity.

Attempting to converge models during this period with extra nickel-mixing proved to be very difficult, and rarely met with success. This likely is another example of the failure of the assumption of homogeneous mixing, as illustrated in the Day 4 model.

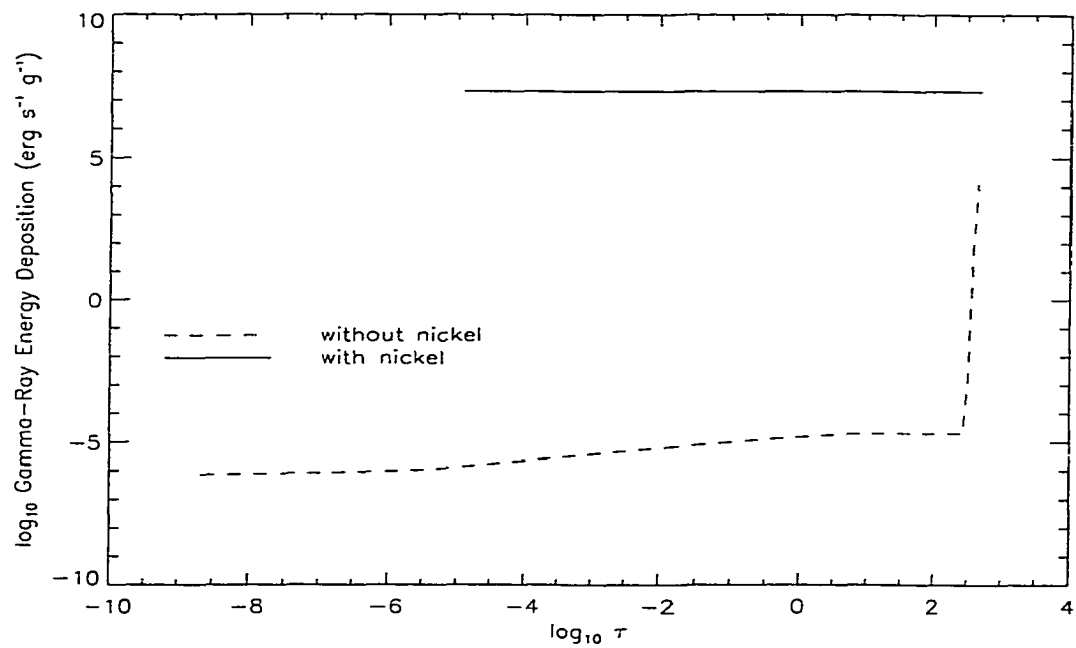


Figure 3.1: Gamma-ray energy deposition vs.  $\tau$  for Day 4.52, Blinnikov et al.'s model, with and without nickel (Blinnikov 1999; Blinnikov et al. 2000).

Table 3.1: Photospheric Temperature

Day	T (K) <sup>1</sup>	$\tau$ <sup>1</sup>
1	12057.2	0.96467
2	8868.4	0.95035
3	7788.0	1.0176
4	7170.1	0.94891
8	6911.6	1.6606 <sup>2</sup>
10	6336.6	0.73683 <sup>2</sup>
14	6353.0	0.80965
18	6722.9	0.97625
24	5880.0	0.84689
30	6947.3	1.1932
58	6486.1	1.5816 <sup>2</sup>
81	6092.3	0.97610
103	6235.0	0.72259 <sup>2</sup>

---

<sup>1</sup>Temperature and  $\tau$  values given are those for the zone in the spectral model for which  $\tau$  is closest to the value 1.00. All models have no alterations from Blinnikov's original parameters.

<sup>2</sup>Low resolution at photosphere.

Table 3.2: Best-Fit Nickel Mass Fractions

Day	Mass Fraction	tapp
1	N/A	N/A
2	N/A	N/A
3	N/A	N/A
4	$1.0 \times 10^{-3}$	N/A
8	$1.0 \times 10^{-4}$	$1.0 \times 10^{-3}$
10	$1.0 \times 10^{-3}$	$1.0 \times 10^{-3}$
14	$1.0 \times 10^{-4}$	$1.0 \times 10^{-3}$

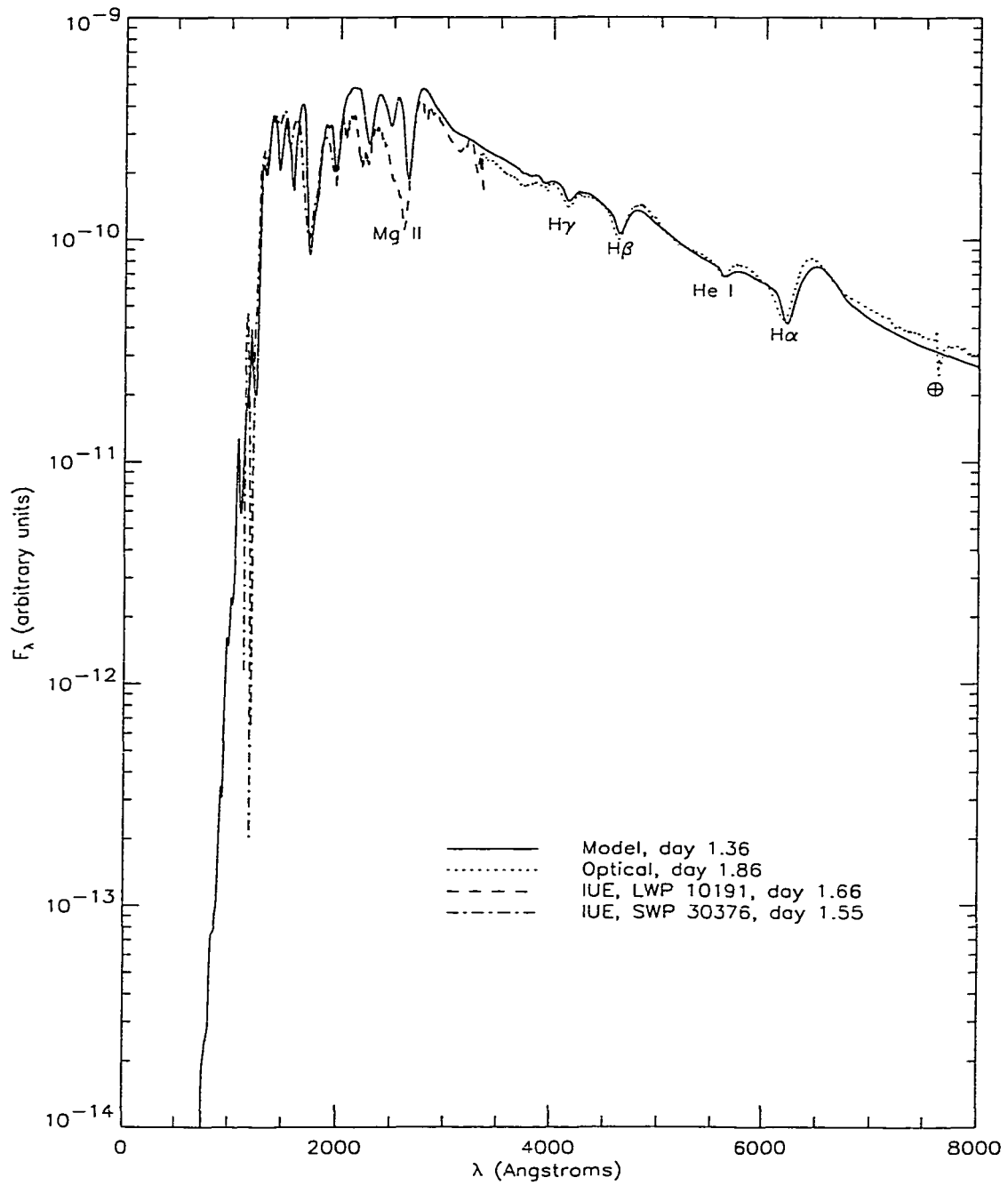


Figure 3.2: PHOENIX model spectrum for Day 1.36.

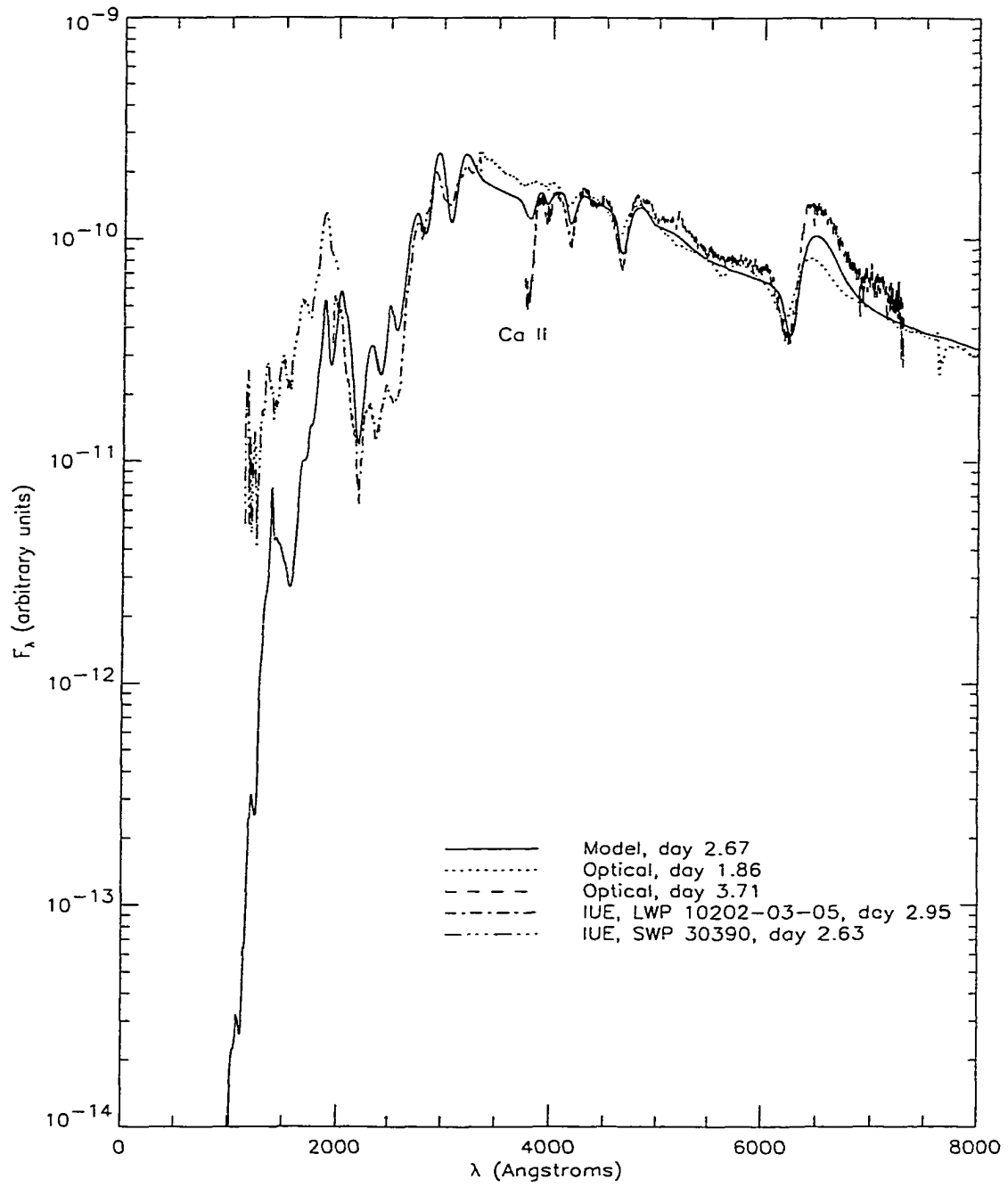


Figure 3.3: PHOENIX model spectrum for Day 2.67.

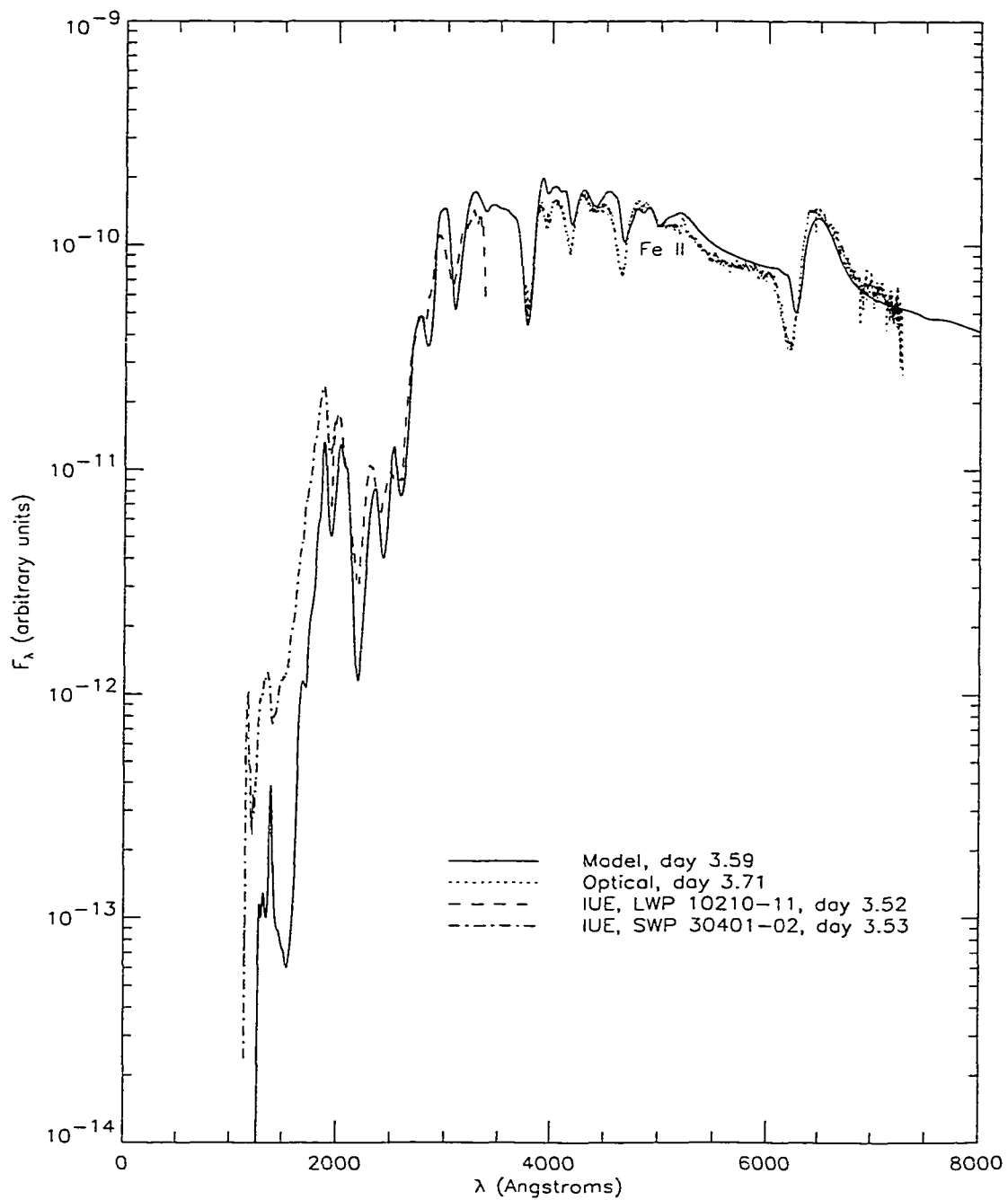


Figure 3.4: PHOENIX model spectrum for Day 3.59.

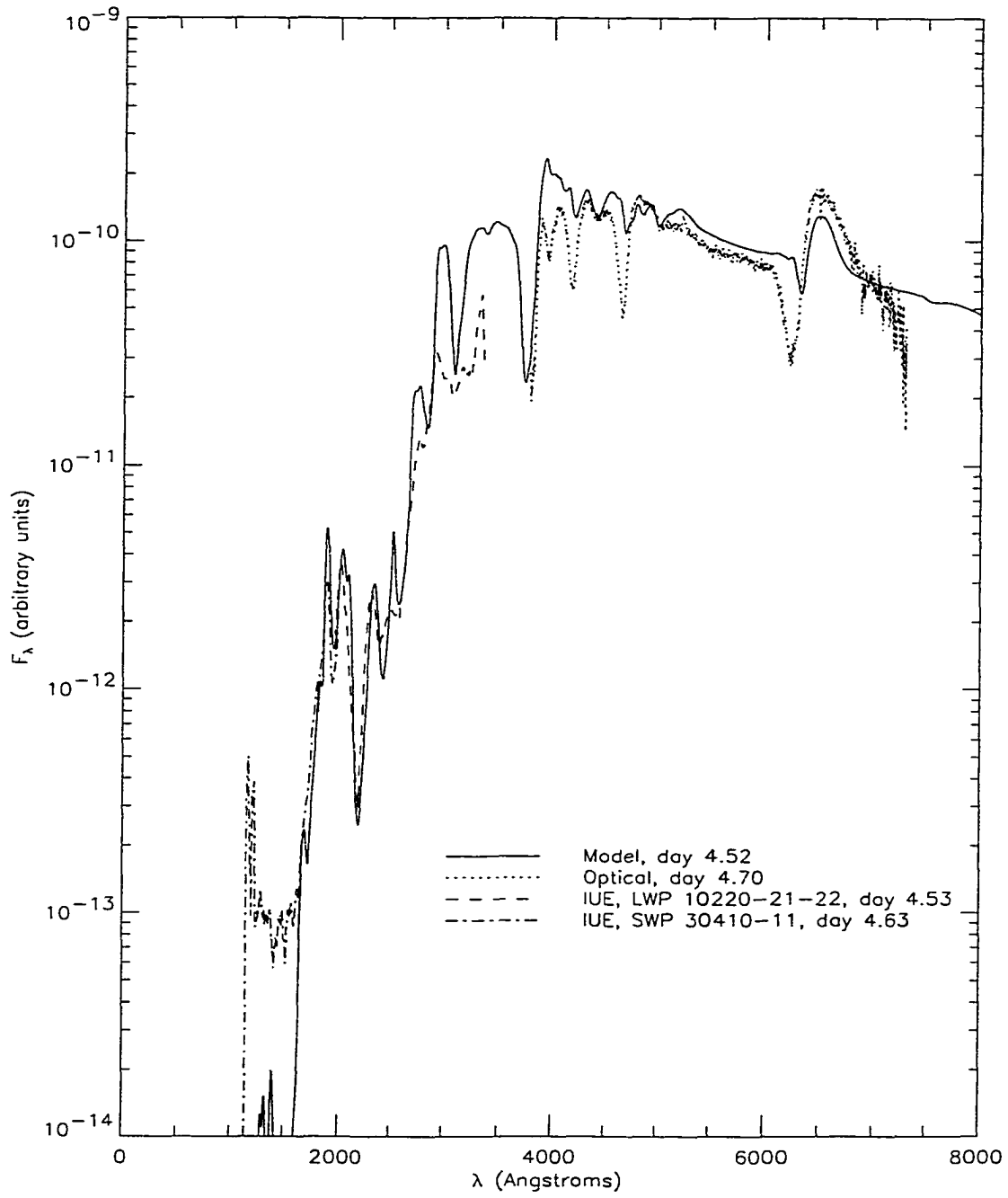


Figure 3.5: PHOENIX model spectrum for Day 4.52, without additional nickel mixing.

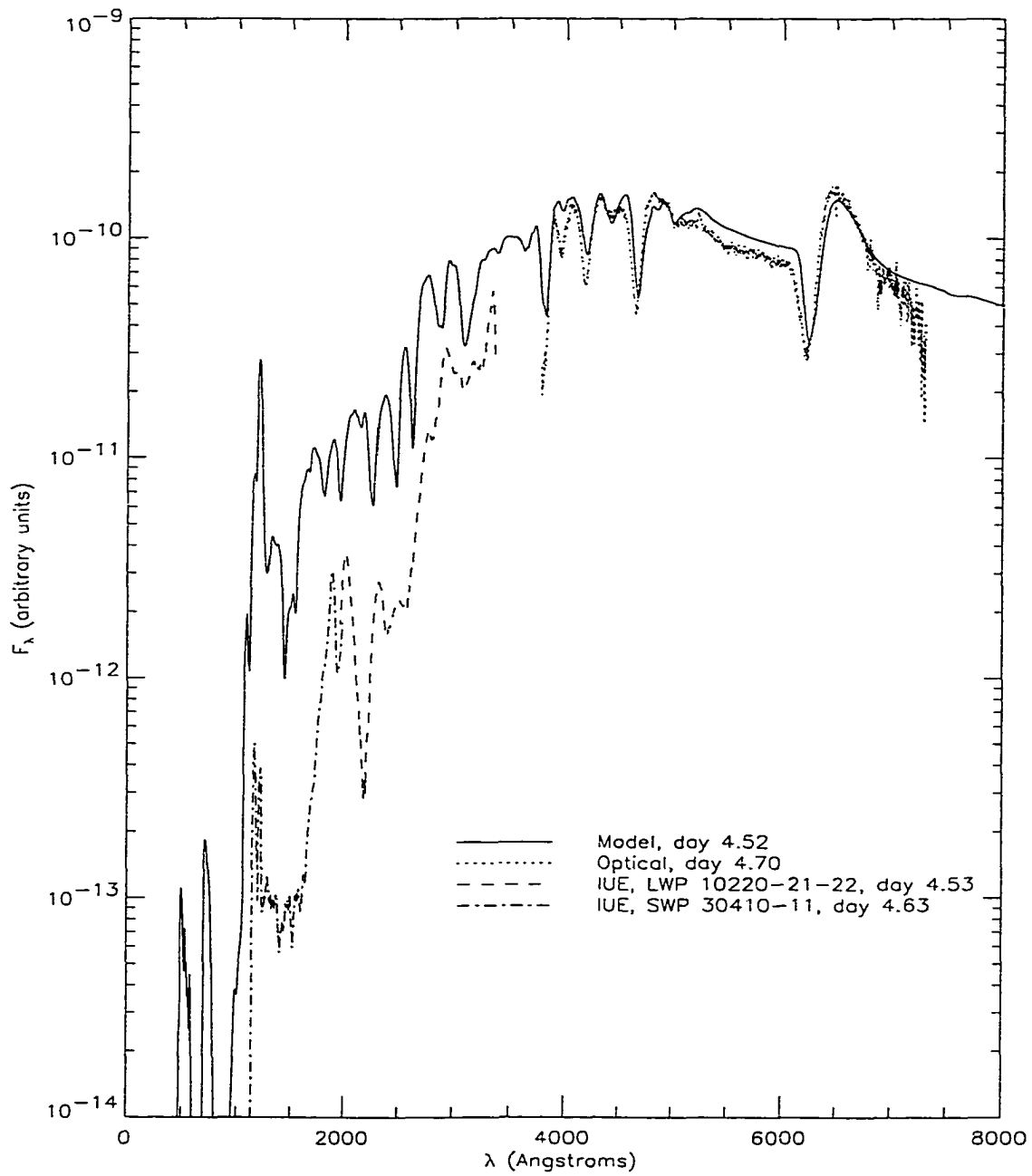


Figure 3.6: PHOENIX model spectrum for Day 4.52, with gamma-ray deposition calculated assuming local deposition due to a constant nickel mass fraction of  $1.0 \times 10^{-3}$  everywhere in the envelope. 75-layer model.

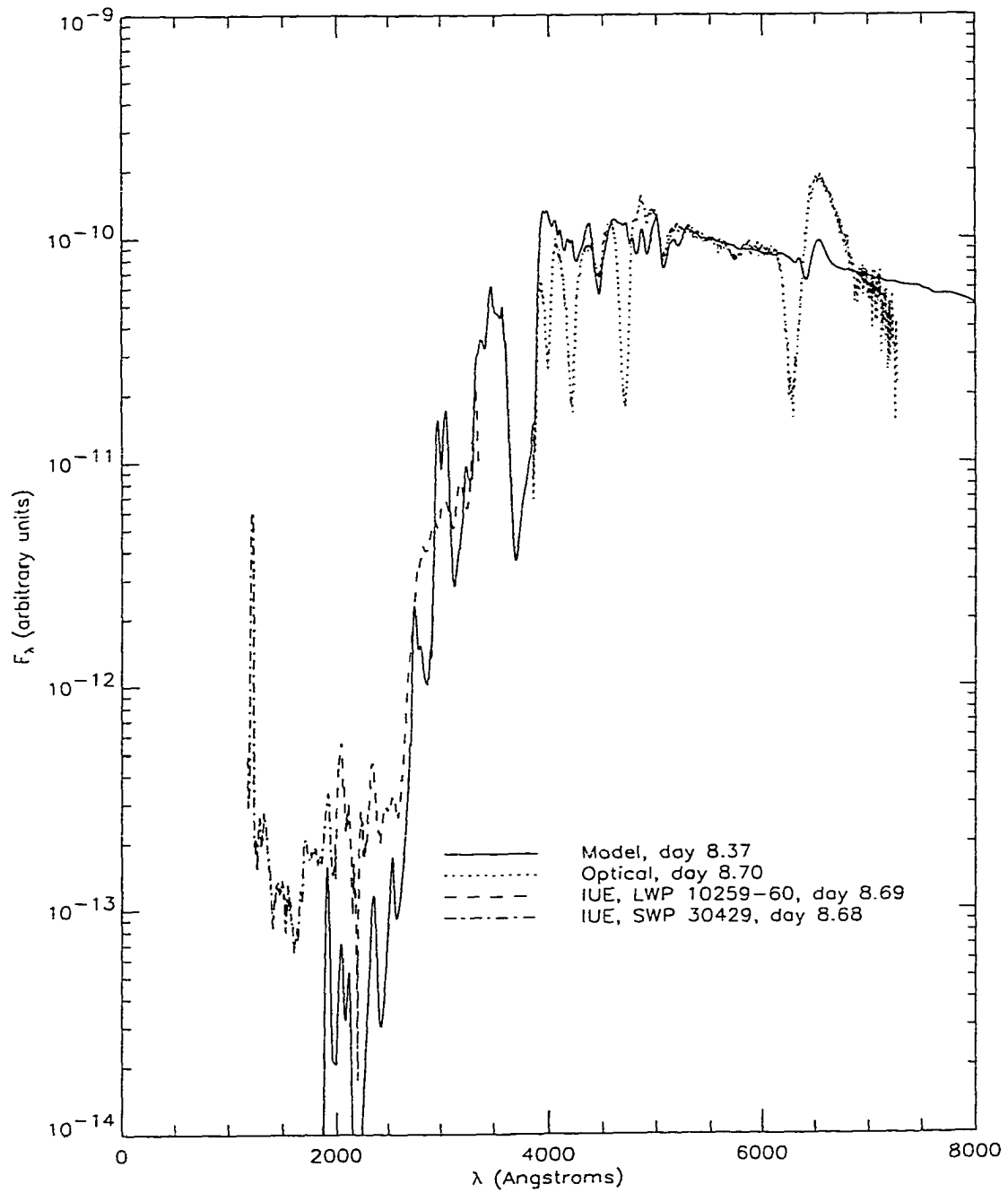


Figure 3.7: PHOENIX model spectrum for Day 8.37, without additional nickel mixing.

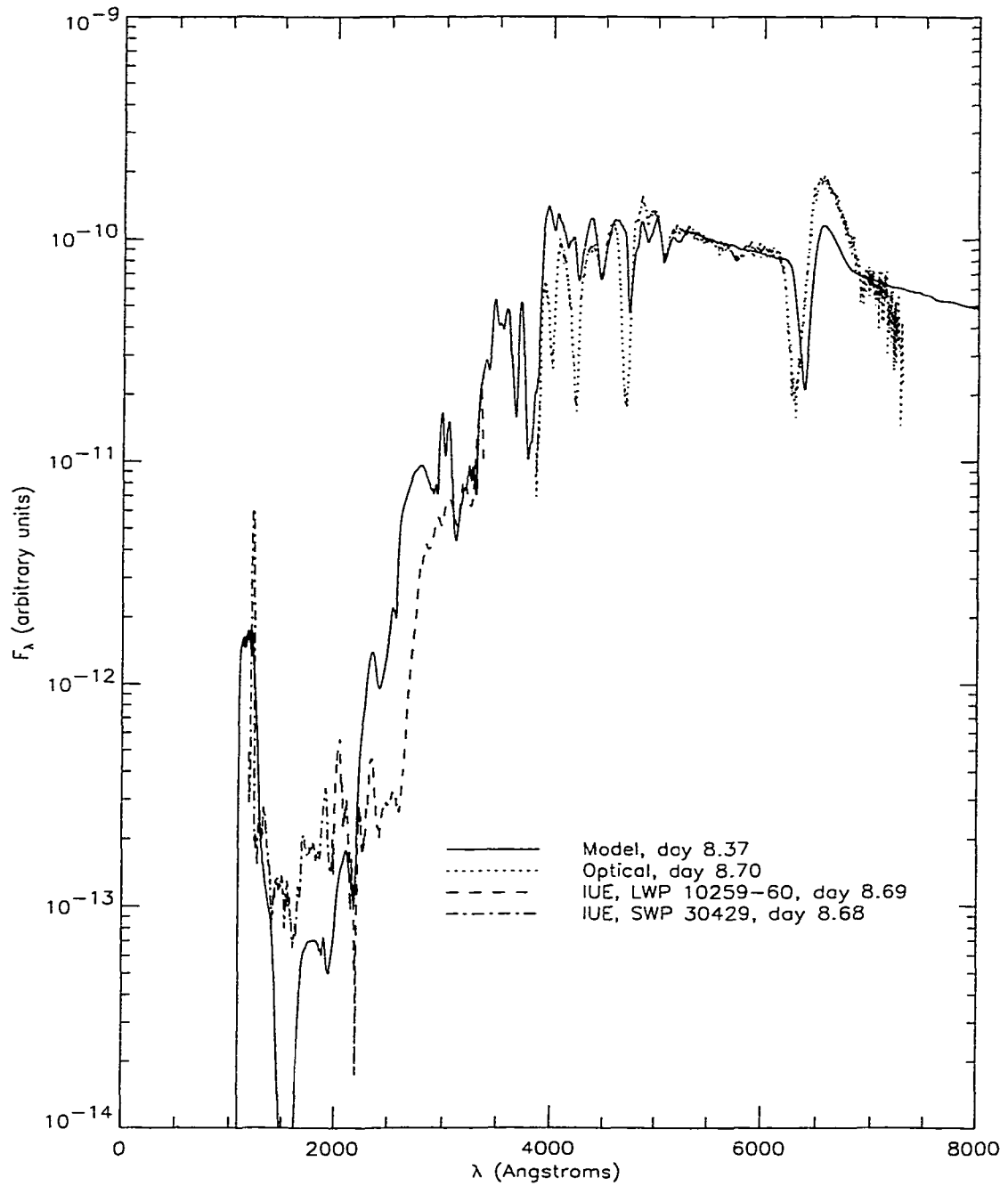


Figure 3.8: PHOENIX model spectrum for Day 8.37, with a nickel mass fraction of  $1.0 \times 10^{-4}$  everywhere in the envelope, and a tapp value of  $1.0 \times 10^{-3}$ .

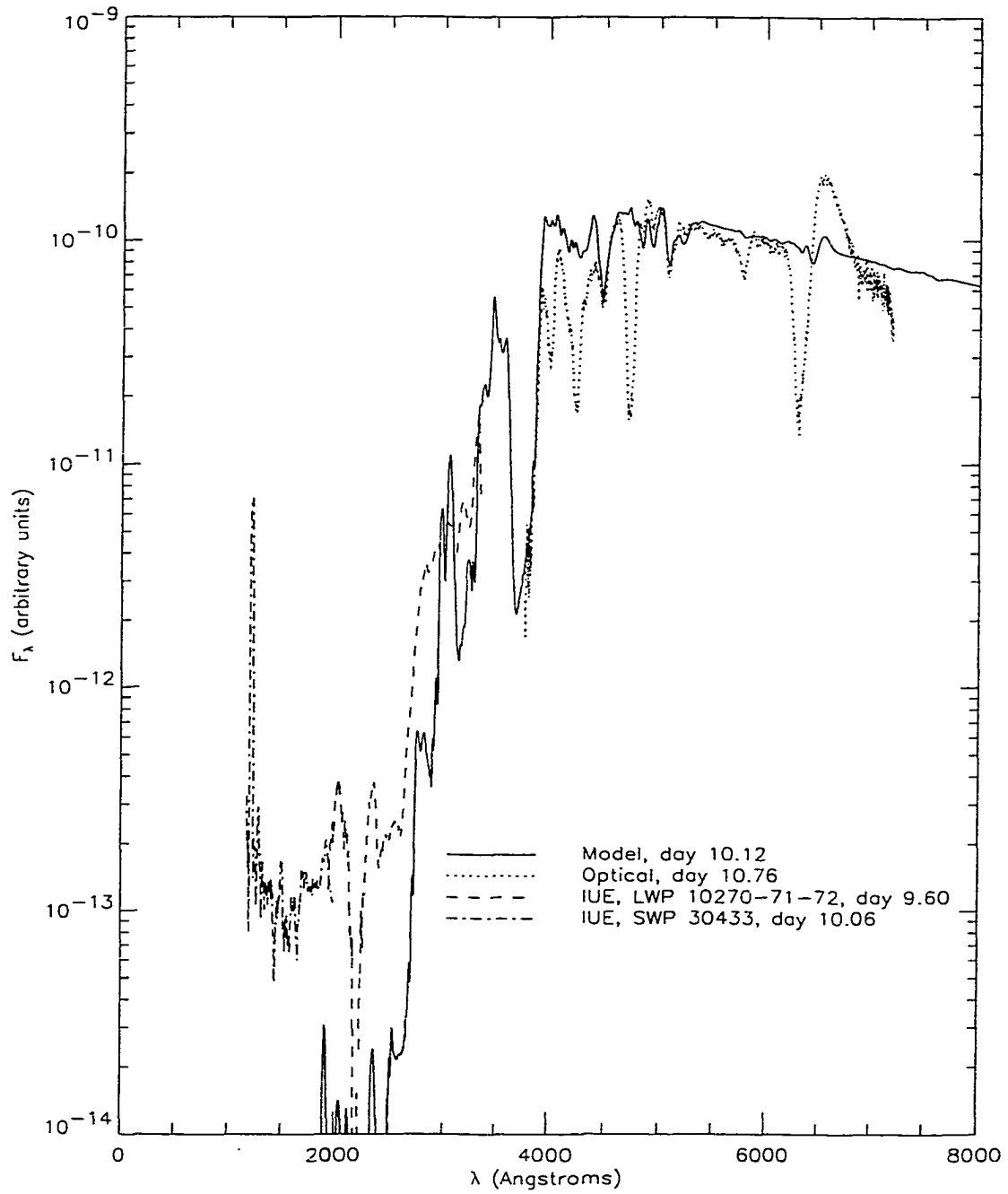


Figure 3.9: PHOENIX model spectrum for Day 10.12, without additional nickel mixing.

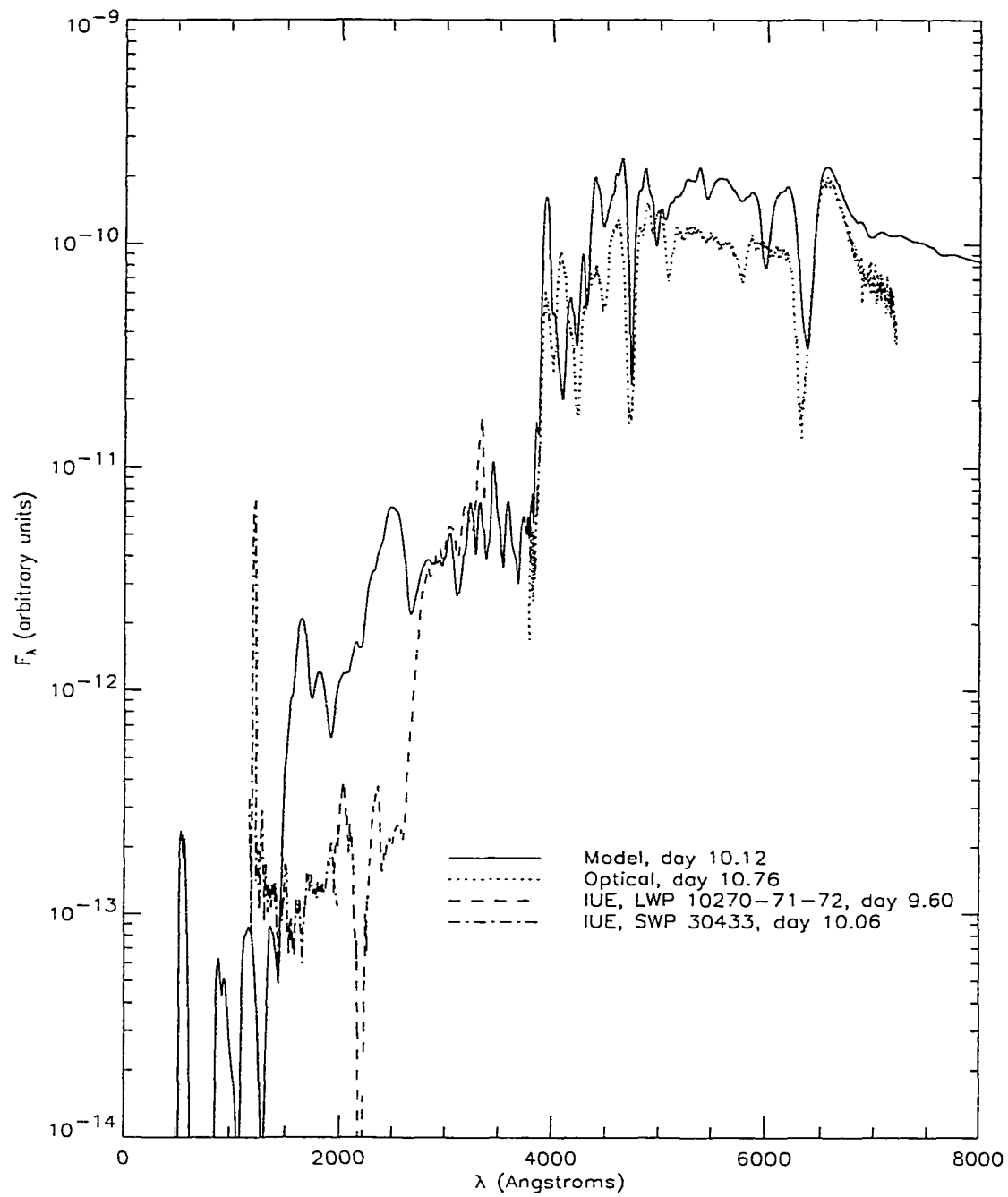


Figure 3.10: PHOENIX model spectrum for Day 10.12, with a nickel mass fraction of  $1.0 \times 10^{-3}$  everywhere in the envelope, and a  $\tau_{\text{app}}$  value of  $1.0 \times 10^{-3}$ .

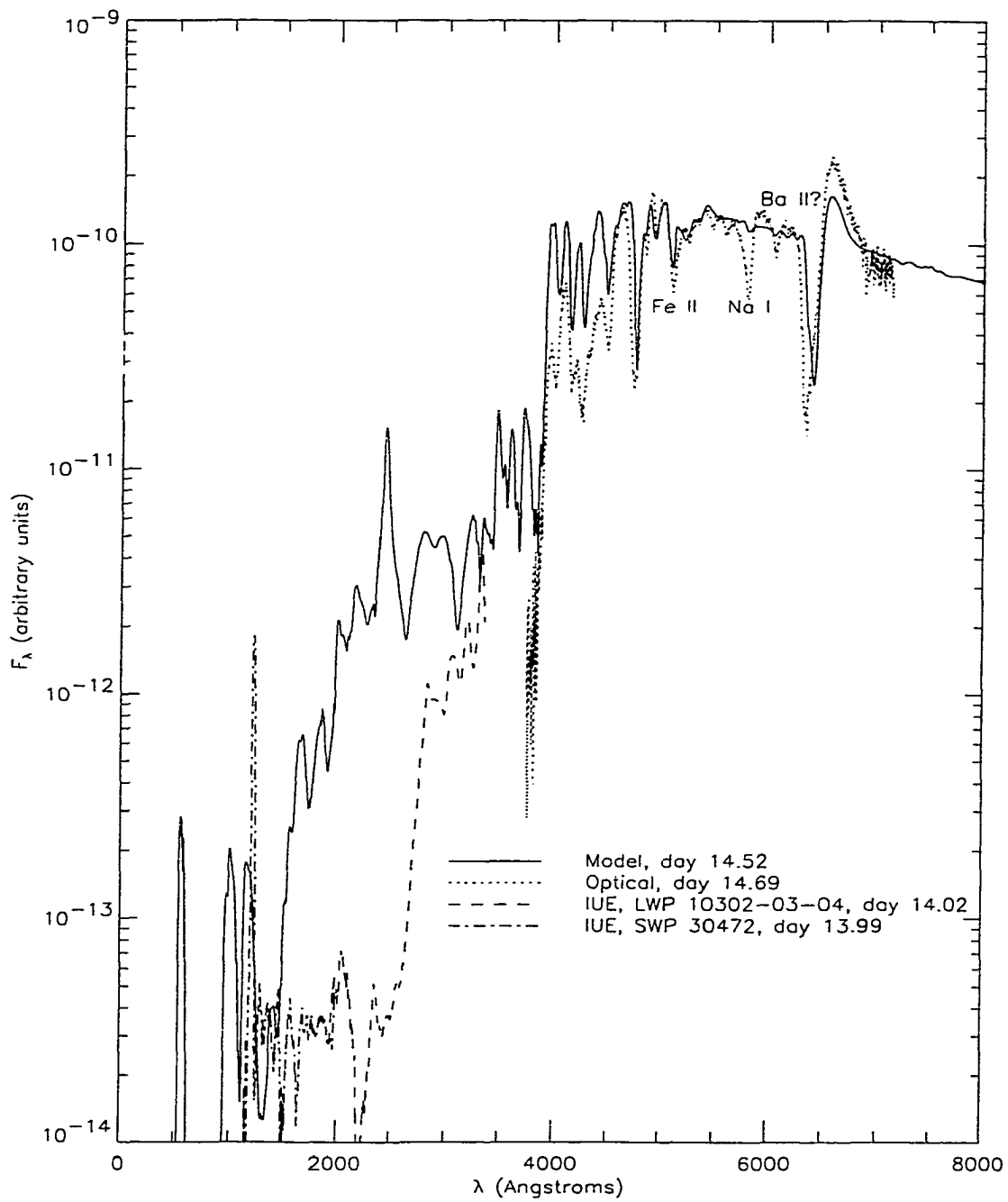


Figure 3.11: PHOENIX model spectrum for Day 14.52, with a nickel mass fraction of  $1.0 \times 10^{-4}$  everywhere in the envelope, and a tapp value of  $1.0 \times 10^{-3}$ . 75-layer model.

# Chapter 4

## Days 18-103

### 4.1 Temperature Profile

One of the first models to be successfully converged in this era was that of Day 58.6, and the results were surprising. Refer to figure 4.5, and note that the Blinnikov spectral model is at least ten times brighter in the red than the observed spectrum indicates. It was theorized that discrepancies in the temperature profile are due to the overexcitation of iron at the specific temperatures given in the model, resulting in excessive cooling and therefore a reddening of the model's envelope. The easiest way to alter the temperature profile of the model is to change the luminosity in the input file. In the PHOENIX models, luminosity is a boundary condition required for the solution of the set of differential equations. Changing the luminosity alters the temperature profile of the envelope in a complicated way, but it is convenient to think of it as changing the model temperature of the synthetic spectrum (e.g. color temperature or effective temperature).

I tried both increasing and decreasing the luminosity in order to observe the effects of changing the model temperature, and it was found that increasing the luminosity, and therefore the temperature, was the correct means to reduce the discrepancy between

the synthetic profile and the observed profile. Figure 4.7 shows the model for Day 58 where the luminosity has been increased 28.0% from the original value, and this gives the correct temperature profile. Each of the Blinnikov models within the period from Day 18 to Day 81 required some increase in luminosity to make the temperature profiles match. The Blinnikov model for Day 103, on the other hand, produces a spectrum that is too dim in the red (figure 4.11), which suggests that a decrease in luminosity may be required to correct it.

Many different PHOENIX runs were conducted with different luminosity values in order to find the best match. In addition to visually matching the synthetic and observed spectra, a  $\chi$ -square comparison was done using a program written for the IDL graphics package, FITSPEC.PRO. Figure 4.1 displays the results of FITSPEC: The probability of the model being a best-fit is plotted against the relative increase in luminosity over the model's base value for all five model days in the period. The curves are not smooth, owing to time constraints limiting the number of luminosity values that could be run, but even so it is difficult to obtain best-fit values from this graph. A straight  $\chi$ -square may not in fact be an ideal tool for this study, so visual inspections were used in conjunction with FITSPEC to estimate the best-fit luminosity values. The results are in Table 4.1. Days 10 and 14 were also tested for luminosity, and it was found that in both cases the original value was the best fit to within the errors indicated.

For Day 18, the spectral model did not converge after 200 accelerated lambda iterations (maximum  $\Delta T/T = -4.77\%$ ), although the production model immediately preceding the spectral model did. The Day 24 model also converged in production but not in spectrum (maximum  $\Delta T/T = -4.62\%$ ). Ideally, we would want the spectral models to converge better than this, but it should have little effect on the spectral output. No corrected value for the luminosity at Day 103 has been obtained as of the writing of this report, so Day 103 is excluded from Table 4.1.

The errors in the color luminosities that are seen in this study reflect the errors in the synthetic light curves produced by Blinnikov and his collaborators (Blinnikov 1999; Blinnikov et al. 2000). Figure 19 of Blinnikov et al. (2000) shows the light curves of Model 14E1 in the V, B, and U bands, and one notes that the synthetic V band is too dim during the period that includes Days 18–81, and too bright during the period including Day 103. In both cases, the maximum difference between the synthetic and observed brightnesses in the V band is small, no more than 0.3 magnitudes, which corresponds to an increase in luminosity that is in the vicinity of the best-fit values obtained here and listed in Table 4.1.

Temperature inversions were an almost constant problem in the models from day 18 to 81 with added nickel, occurring so frequently that it was often necessary to rezone the model and readjust the temperature profile every few iterations. This is due to the fact that the gamma-ray deposition function should more closely mimic the self-consistent gamma-ray deposition function and therefore we consider models which are for adjusted luminosity only with the self-consistent gamma-ray deposition function of Blinnikov. As we showed at early times, this is likely not the correct deposition function but the parameter space is too large to explore and it is better for us to instruct the hydro modellers to alter their models than for us to search in an enormous parameter space.

## 4.2 Days 18–24

Refer to Figures 4.2 and 4.3. It is clear that nickel-mixing continues to be necessary at this stage in the supernova’s evolution, as evidenced by the almost nonexistent hydrogen lines in the model spectra. The combined Na I  $\lambda$ 5890,5896 line is also not reproduced in the model. Ba II was not calculated in non-LTE in the models, which may account

for why the Ba II line also does not show up, but it is more likely that the barium abundance should be enhanced (due to s-process nucleosynthesis).

Note that the blue portion of the model spectra appear to be too bright, while the red and near-ultraviolet spectra match very well. The reason for this is unknown.

### 4.3 Days 30–81

At Day 58 (see Figures 4.5–4.8), we see the effect of the luminosity parameter on the temperature profile of the spectrum. By this period,  $^{56}\text{Ni}$  has mostly decayed and is no longer producing excess gamma rays, and as can be seen in Figure 4.4, the synthetic Balmer lines have reappeared and are now as strong as the observed lines without the need for extra nickel-mixing. In Figures 4.7 and 4.9, note that in fact the synthetic  $\text{H}\alpha$  line at Days 58 and 81 appears to be too strong.

The observed far-UV spectra of Days 58 and 81 (see Figures 4.8 and 4.10) do not appear to match the synthetic spectra, despite the fact that the near-UV spectra match very well. This may be due to calibration errors in the original spectroscopic data.

### 4.4 Day 103

The model spectrum for Day 103 with Blinnikov’s original luminosity value, shown in Figure 4.11, is much too blue. As of the writing of this work, attempts to correct this by changing the luminosity parameter have been unsuccessful.

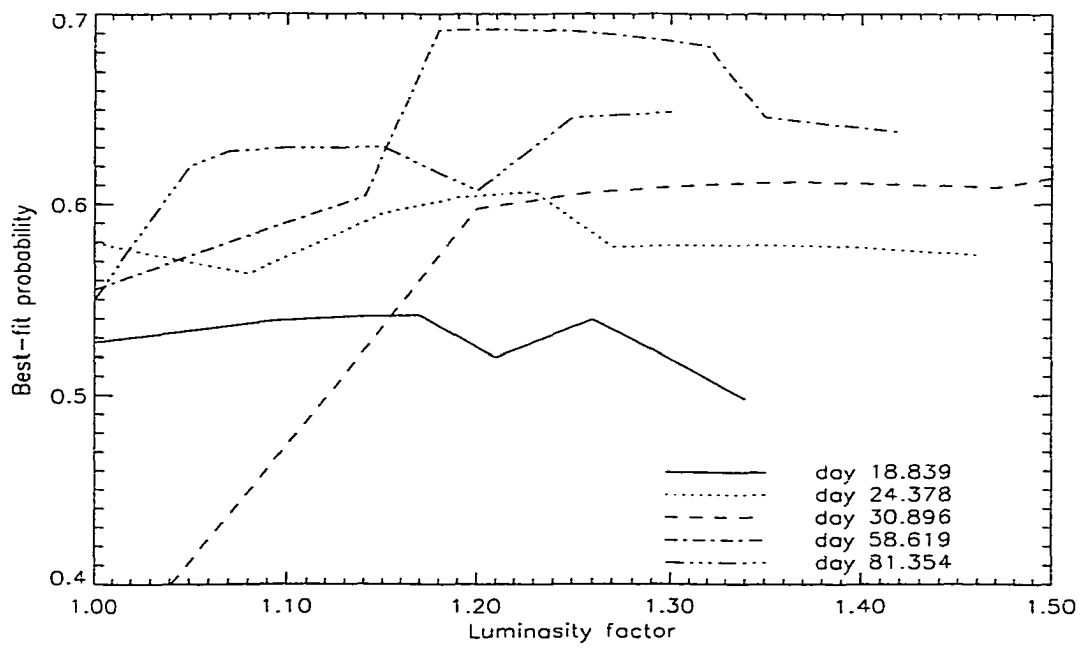


Figure 4.1: Probability of best-fit vs. relative increase in luminosity from model's base value, according to FITS.PRO.

Table 4.1: Required Changes in Luminosities

Day	original L (erg s <sup>-1</sup> )	best-fit L (erg s <sup>-1</sup> )	increase	error
10	$9.26 \times 10^{38}$	$9.26 \times 10^{38}$	0.0%	5.0%
14	$1.03 \times 10^{39}$	$1.03 \times 10^{39}$	0.0%	4.8%
18	$1.17 \times 10^{39}$	$1.42 \times 10^{39}$	21.3%	4.3%
24	$1.30 \times 10^{39}$	$1.75 \times 10^{39}$	34.7%	7.7%
30	$1.53 \times 10^{39}$	$2.08 \times 10^{39}$	36.0%	3.2%
58	$2.86 \times 10^{39}$	$3.66 \times 10^{39}$	28.0%	1.8%
81	$4.01 \times 10^{39}$	$4.36 \times 10^{39}$	8.7%	2.5%

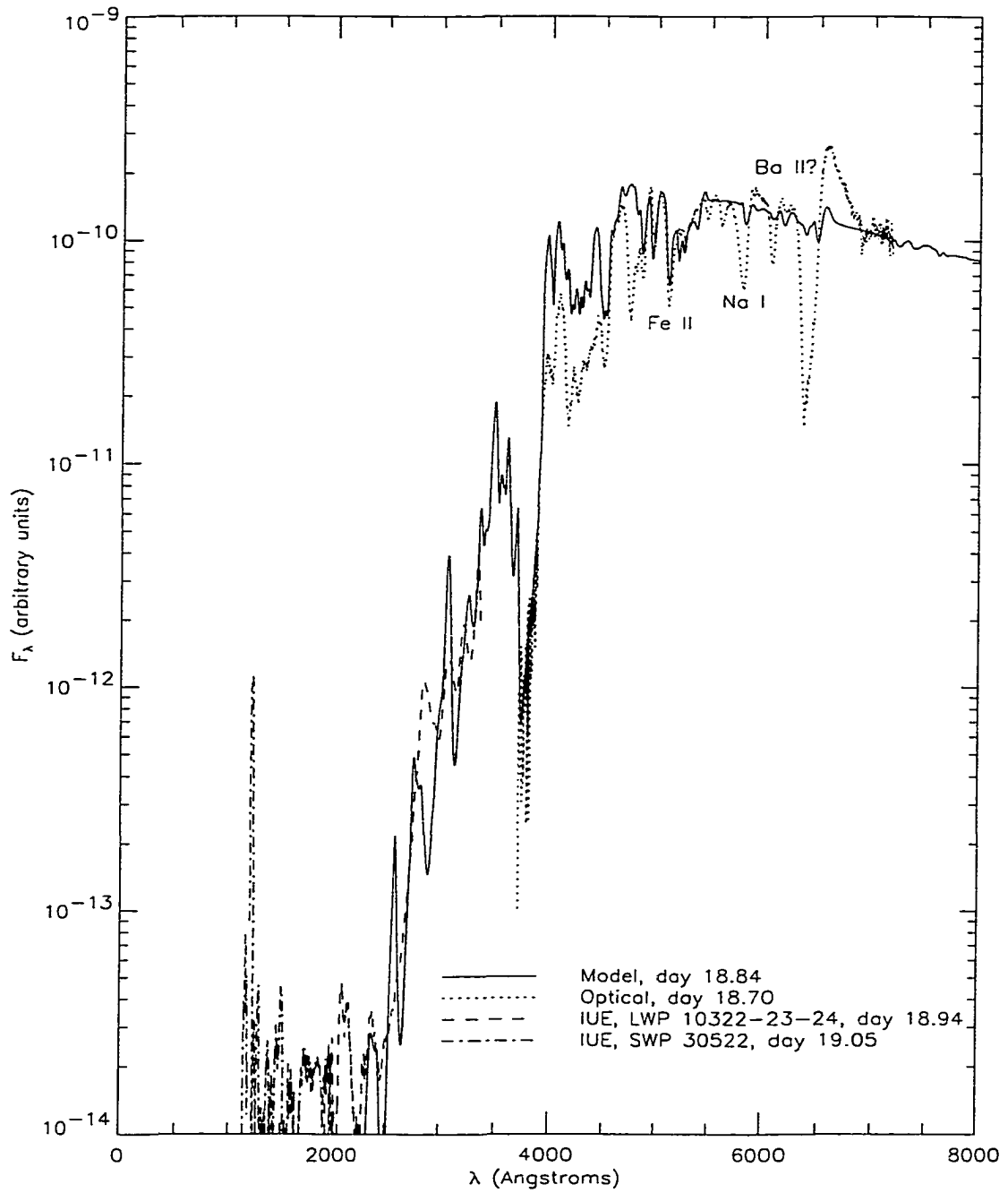


Figure 4.2: PHOENIX model spectrum for Day 18.70, with an increase in luminosity of 21.3% from Blinnikov's original value. No additional nickel mixing.

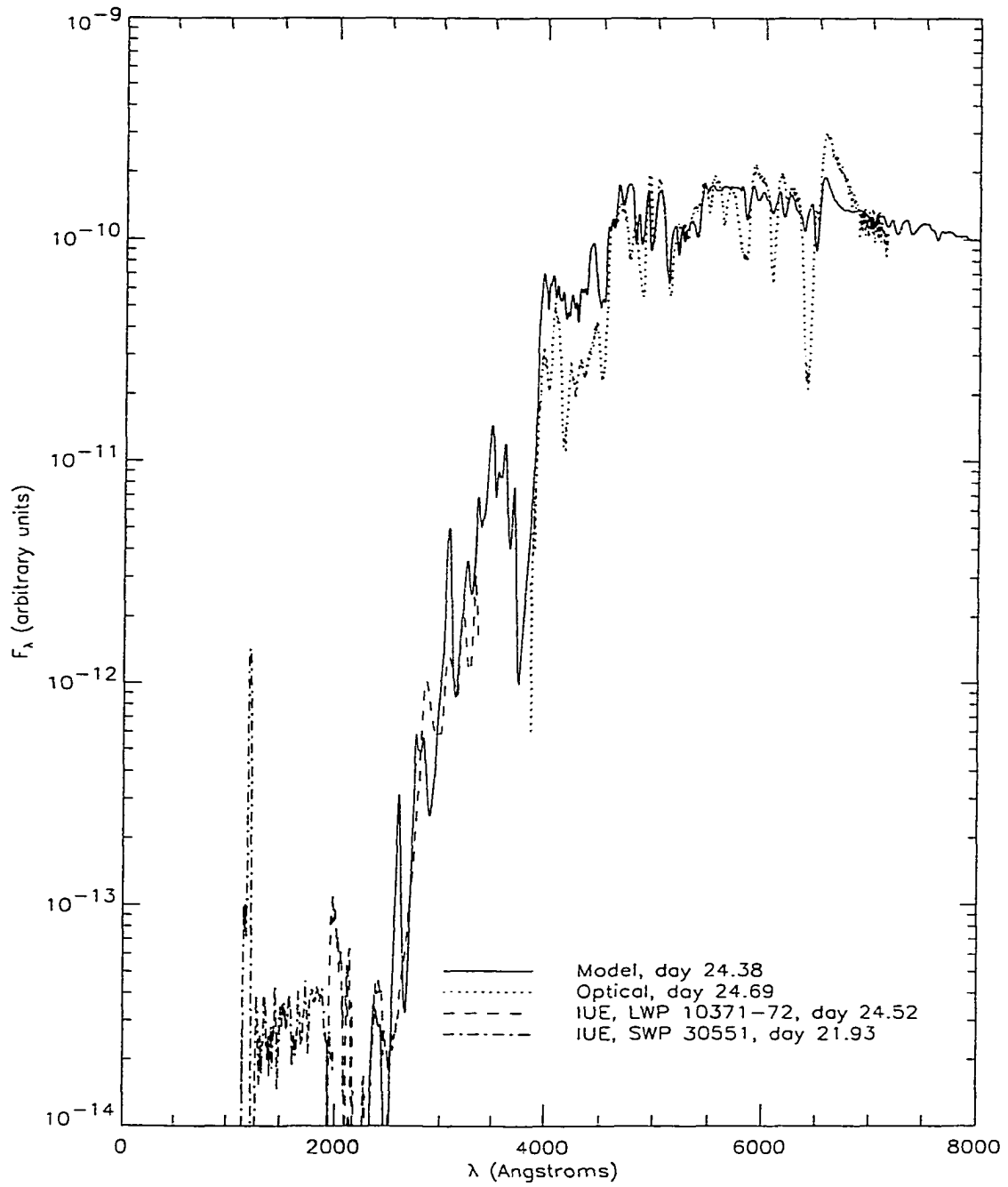


Figure 4.3: PHOENIX model spectrum for Day 24.38, with an increase in luminosity of 34.7% from Blinnikov's original value. No additional nickel mixing.

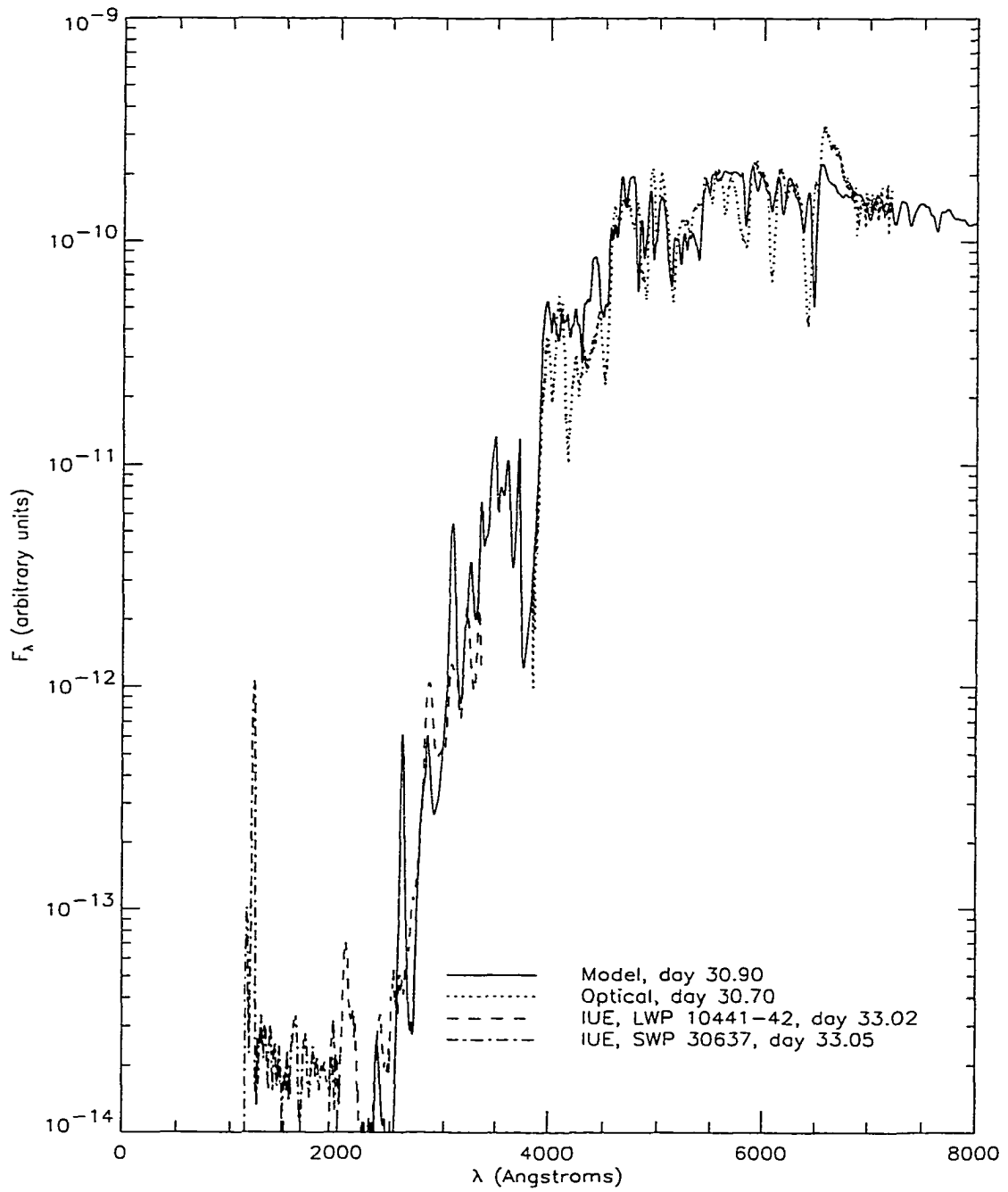


Figure 4.4: PHOENIX model spectrum for Day 30.90, with an increase in luminosity of 36.0% from Blinnikov's original value. No additional nickel mixing.

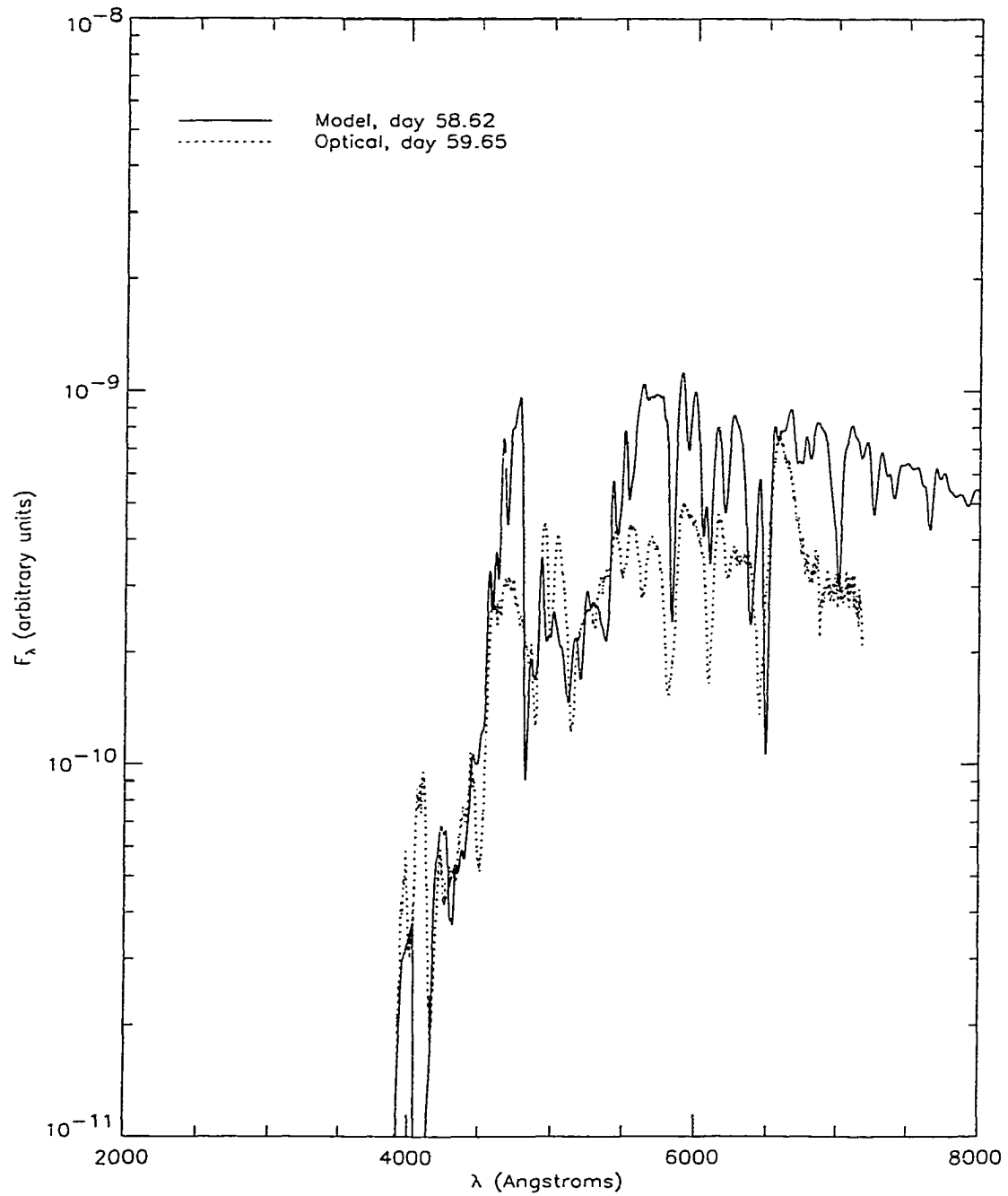


Figure 4.5: PHOENIX model optical spectrum for Day 58.62, with Blinnikov's original luminosity value. No additional nickel mixing.

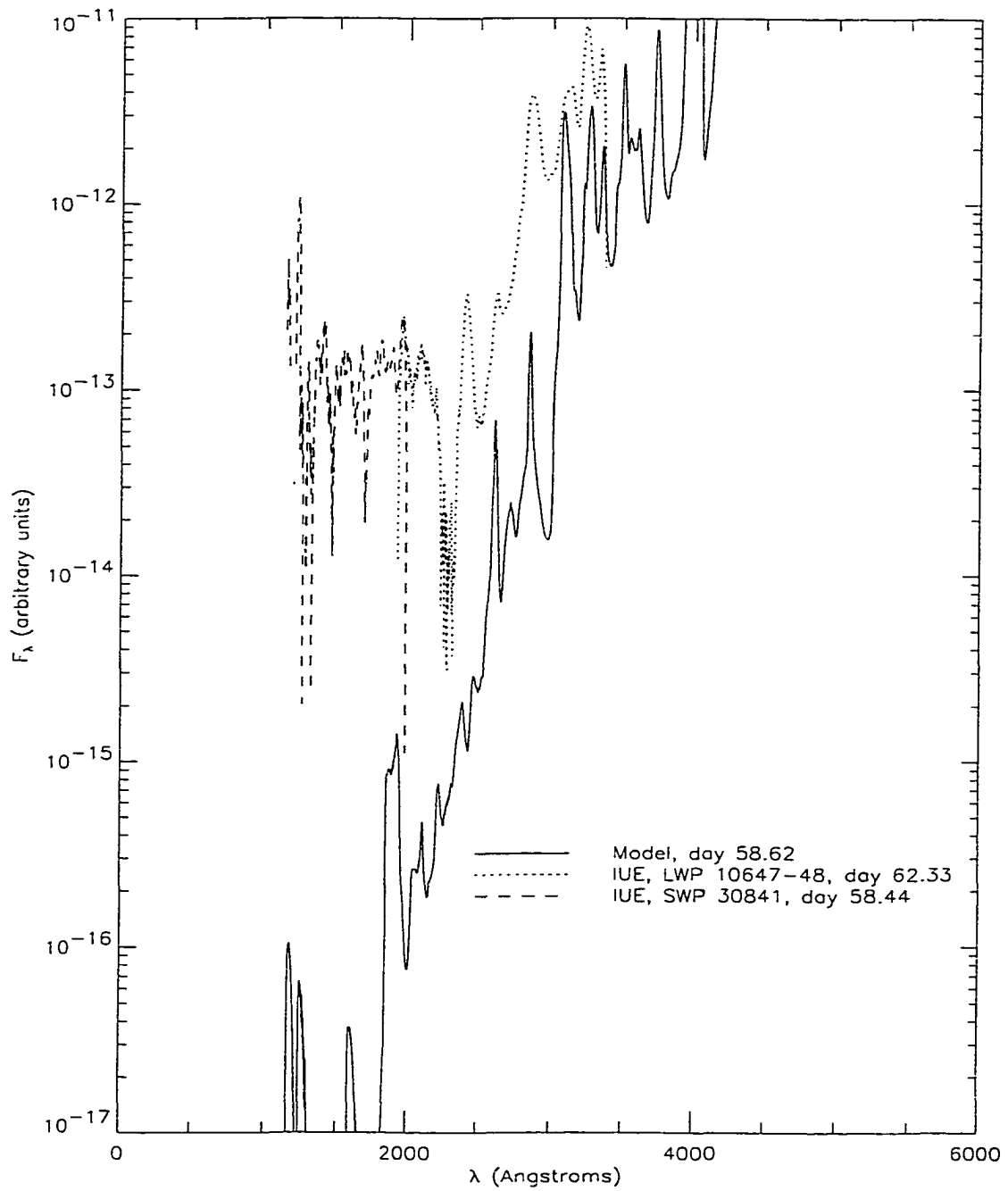


Figure 4.6: PHOENIX model UV spectrum for Day 58.62, with Blinnikov's original luminosity value. No additional nickel mixing.

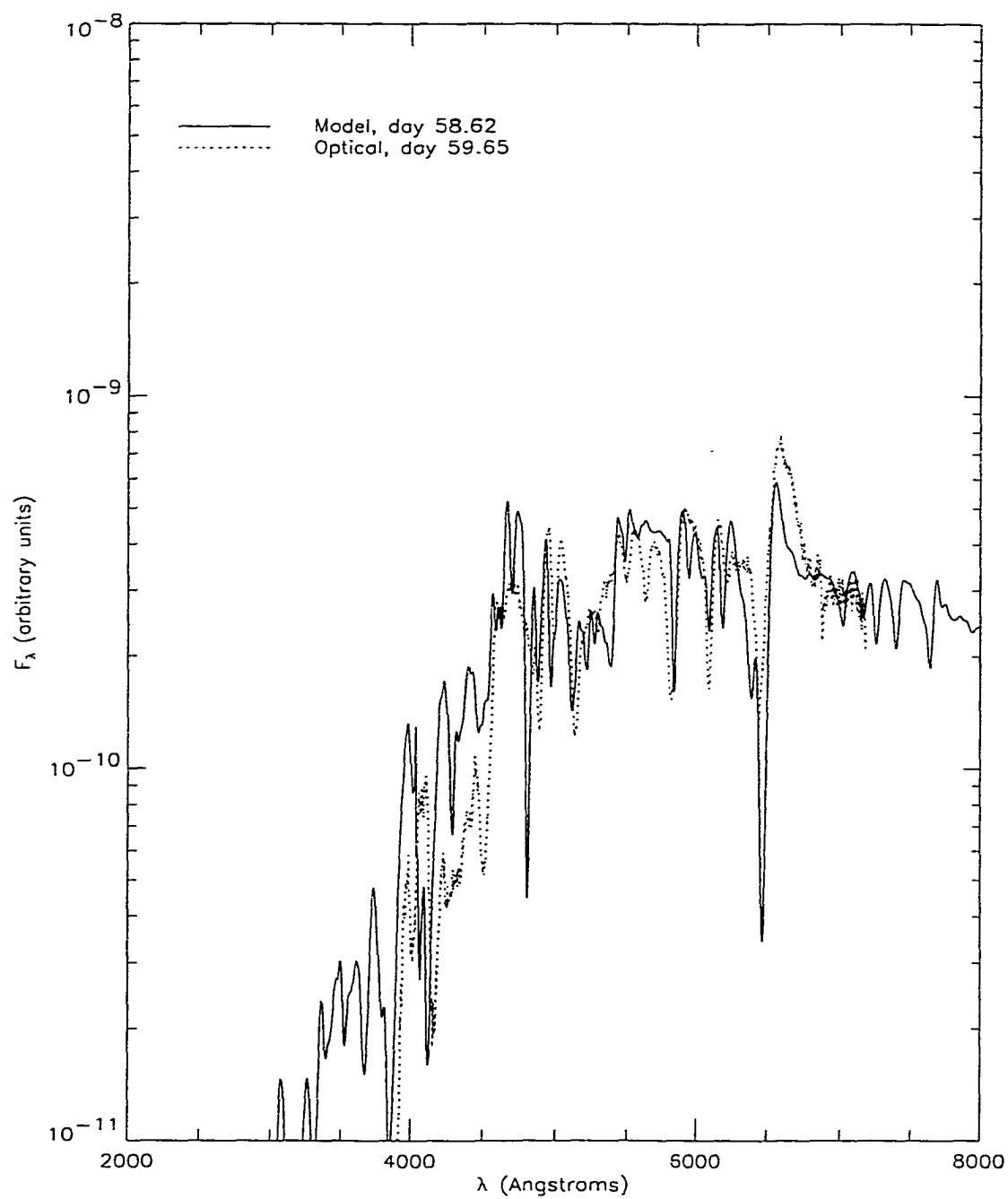


Figure 4.7: PHOENIX model optical spectrum for Day 58.62 with an increase in luminosity of 28.0% from Blinnikov's original value. No additional nickel mixing.

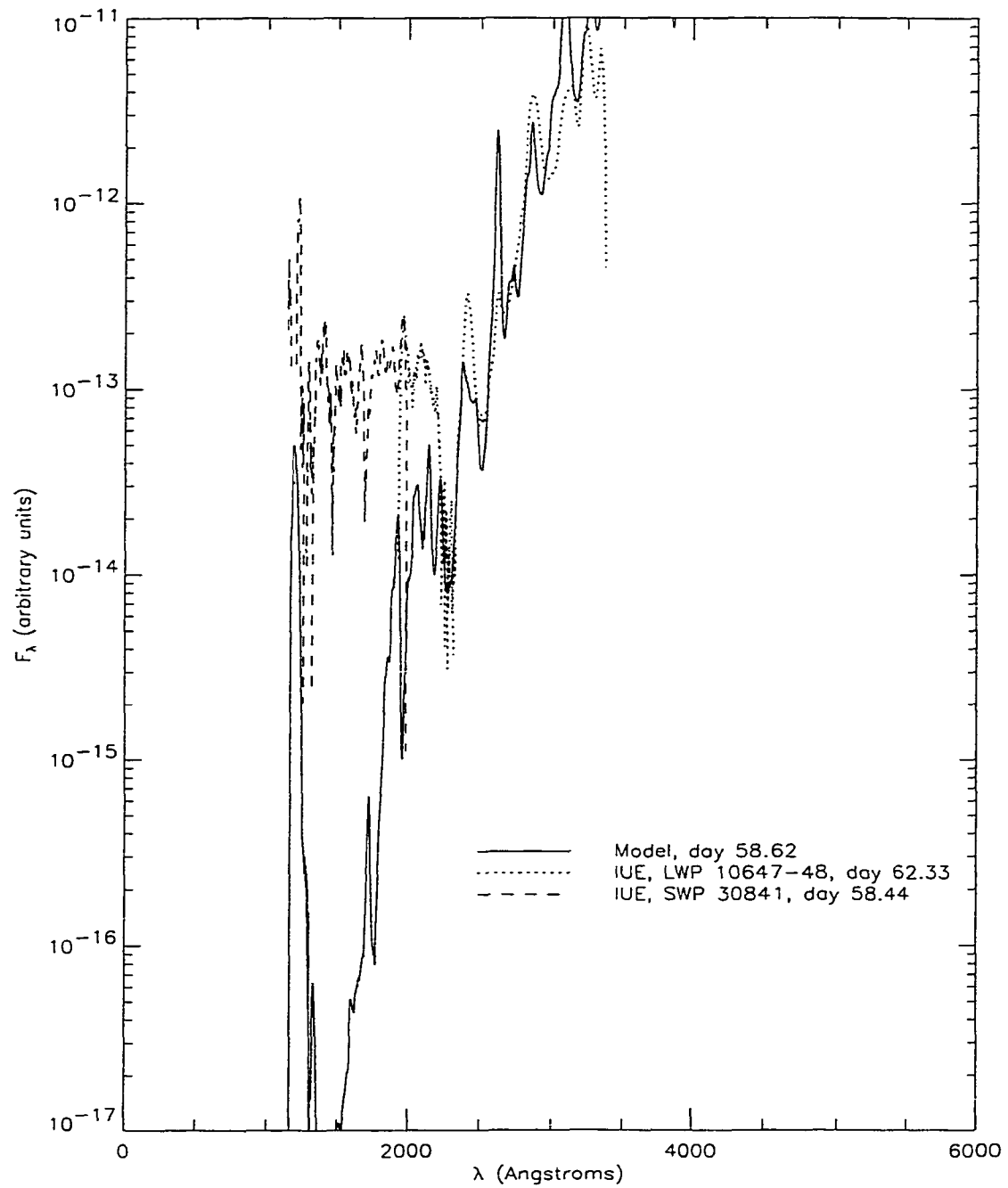


Figure 4.8: PHOENIX model UV spectrum for Day 58.62, with an increase in luminosity of 28.0% from Blinnikov's original value. No additional nickel mixing.

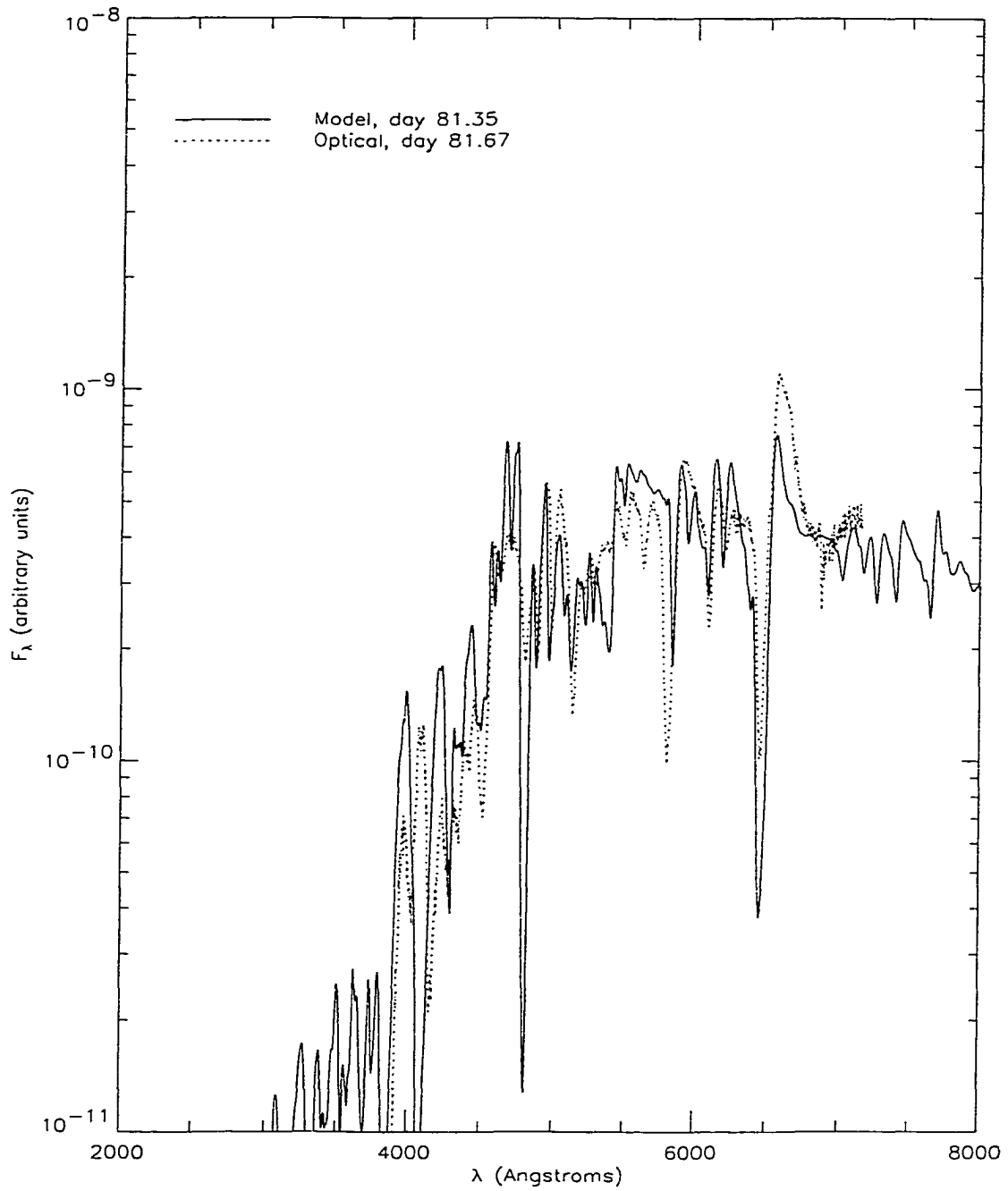


Figure 4.9: PHOENIX model optical spectrum for Day 81.35, with an increase in luminosity of 8.7% from Blinnikov's original value. No additional nickel mixing.

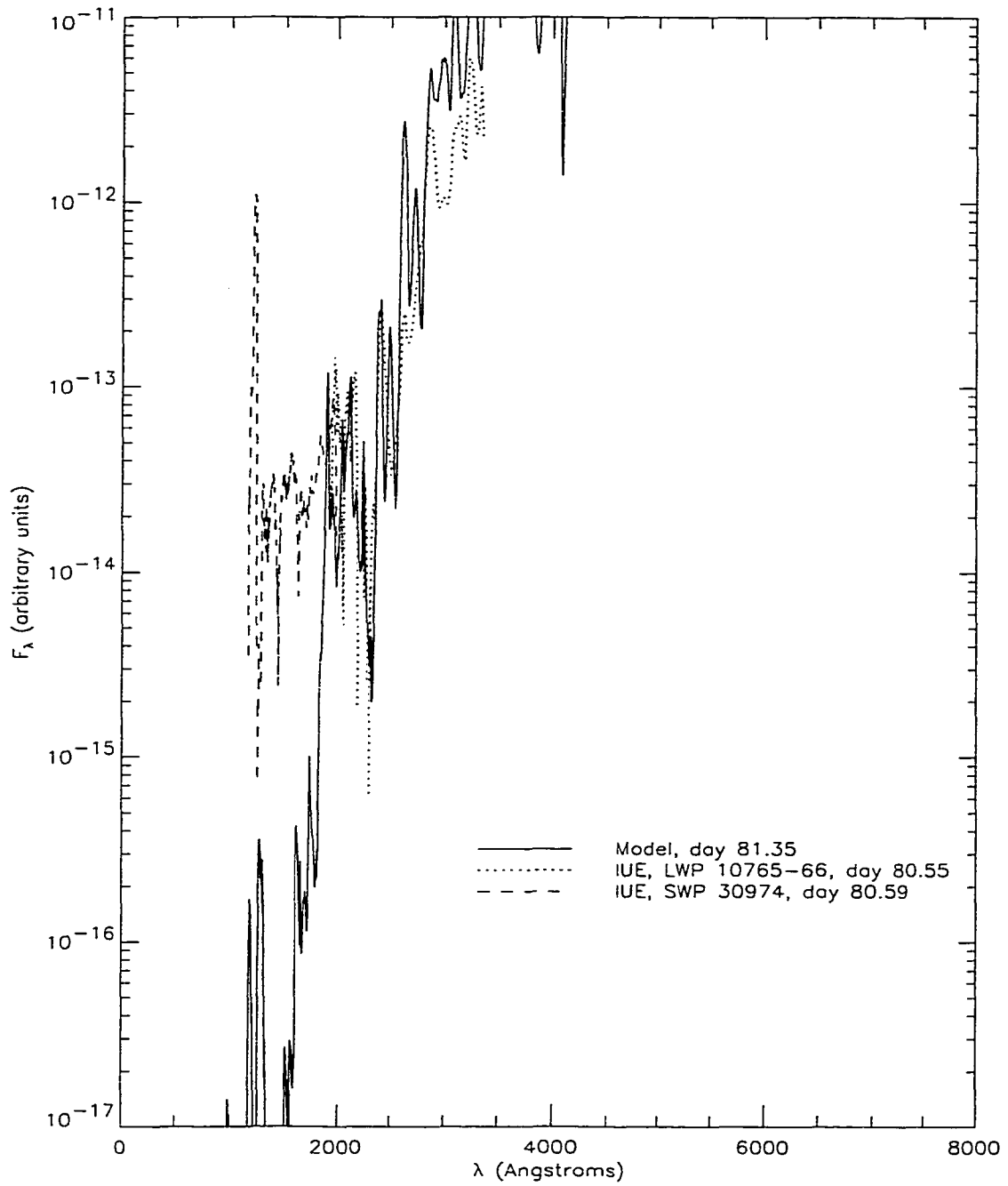


Figure 4.10: PHOENIX model UV spectrum for Day 81.35, with an increase in luminosity of 8.7% from Blinnikov's original value. No additional nickel mixing.

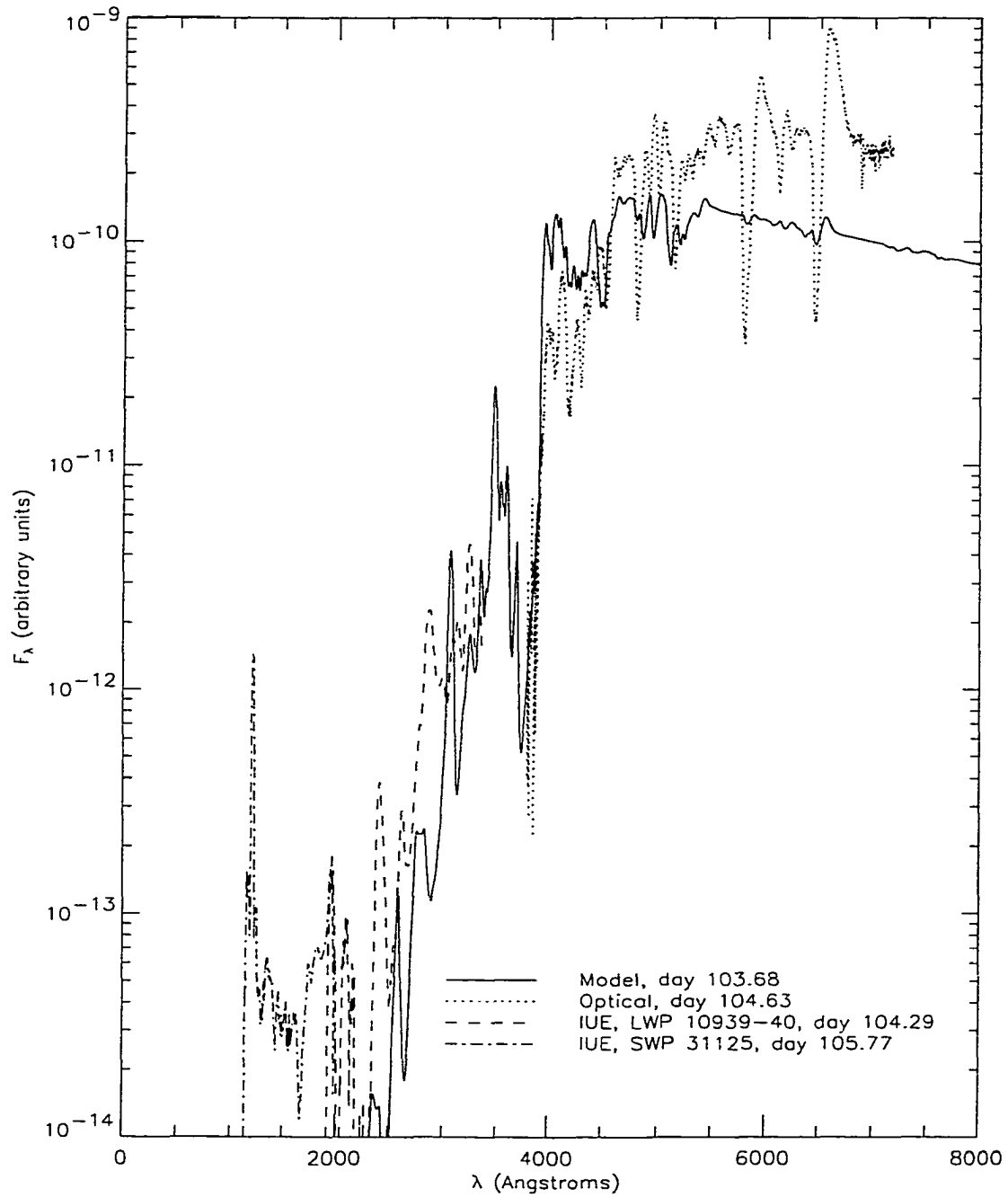


Figure 4.11: PHOENIX model spectrum for Day 103.68, with Blinnikov's original luminosity and no additional nickel mixing.

## Chapter 5

# Distance Measurement

### 5.1 The PHOENIX Distance

Table 5.1 lists all the best-fit models for Days 1–81, their bolometric luminosities, and their absolute UBVR magnitude. Color magnitudes were calculated with a program that uses filter functions from Cardelli et al. (1989), with an  $E_{B-V}$  of 0.16 applied (Lundqvist and Fransson 1996). Table 5.2 shows the corresponding apparent color magnitudes of 1987A, not dereddened, and Table 5.3 gives the resulting distance moduli  $\mu$  and their errors. Errors were calculated based upon inherent errors in apparent color magnitudes, errors between models with and without nickel-mixing for each given day that applies, and errors in the best-fit luminosity for each applicable day.

Figure 5.1 displays the distance moduli vs. day and produces three best-fit averages, one including all bands, another excluding the data from Days 18 and 24, and a third excluding the U-band data. Based upon these average moduli and their errors, and using the formula  $d = 10^{(\mu+5)/5}$  (d in pc), the distance to SN 1987A is  $52.61 \pm 6.27$  kpc (all data). If we ignore the models for Days 18 and 24, the distance is  $51.90 \pm 6.19$  kpc. If we also ignore the U-band data, the distance is  $50.26 \pm 3.70$  kpc. Given the higher

uncertainties in both the U-band photometry and the moduli, this is not unreasonable.

## 5.2 Other Distances

Eastman and Kirshner (1989) used a code to solve the NLTE equations of statistical equilibrium and the time-independent radiation transport equation in Woosley's model atmosphere (Woosley 1988) for five intervals from Day 1 to Day 10. Eastman and Kirshner used a power-law density structure, a He mass fraction of  $0.4 \leq Y \leq 0.9$ , and set  $\xi = 0.8$  after  $t = 7$  days. The distance they derived for 1987A was  $49 \pm 6$  kpc ( $\mu = 18.45 \pm 0.28$ ). Branch (1987) used the Expanding Photosphere Method to obtain a distance of  $55 \pm 5$  kpc, assuming  $\xi = 1$ .

As the ejecta from 1987A continued to expand, it encountered a ring of circumstellar material, probably ejected from the progenitor star years before, and began to illuminate it. This afforded astronomers an opportunity to take advantage of the "light echo" between the foreground and background portions of the ring to calculate a distance to the supernova. The illumination of the ring begins at:

$$t_0 = (R_{ring}/c)(1 - \sin i),$$

where  $R$  is the absolute radius and  $i$  is its inclination to the line of sight, and reaches a maximum at:

$$t_{max} = (R_{ring}/c)(1 + \sin i),$$

thereby allowing both  $i$  and  $R_{ring}$  to be determined independently.

Panagia et al. (1991) used HST ring images and IUE UV light curves to determine angular and absolute radii, and used  $t_0 = 83 \pm 6$  days and  $t_{max} = 413 \pm 24$  days, and assumed the ring is circular. Their resulting distance estimate was  $51.2 \pm 3.1$  kpc

( $\mu = 18.50 \pm 0.13$ ), later refined to  $50.9 \pm 1.8$  kpc (Panagia et al. 1997). Gould (1995) also assumed a circular ring but obtained lower values of  $t_0$  and  $t_{max}$  from the light curves ( $t_0 = 75.0 \pm 2.6$  days,  $t_{max} = 390.0 \pm 1.8$  days) and calculated an upper limit of  $46.77 \pm 0.76$  kpc to the supernova. Gould and Uza (1998) used light echo calculations that accounted for the possibility of an elliptical ring. Their calculations obtained  $\mu < 18.37 \pm 0.04$  for the case of a circular ring, and  $\mu < 18.44 \pm 0.05$  for an elliptical ring. A list of 1987A distances from other sources can be found in Table 5.5.

Table 5.1: Models, Best-fit Luminosities

Day	†	JD 2446800+	$L_{bol}$ (erg s <sup>-1</sup> )	$L_{bol}$ error	$M_U$	$M_B$	$M_V$	$M_R$	$M_I$
1	wo	51.255	$1.95 \times 10^{39}$	N/A	-14.33	-13.57	-13.67	-13.91	-14.02
2	wo	52.556	$1.32 \times 10^{39}$	N/A	-14.19	-13.67	-13.92	-14.24	-14.40
3	wo	53.483	$1.15 \times 10^{39}$	N/A	-13.81	-13.65	-14.02	-14.33	-14.52
4	w	54.415	$1.05 \times 10^{39}$	N/A	-13.34	-13.33	-13.97	-14.35	-14.57
4	wo	54.415	$1.05 \times 10^{39}$	N/A	-13.48	-13.57	-13.99	-14.33	-14.56
8	w	58.265	$9.67 \times 10^{38}$	N/A	-12.76	-13.47	-14.21	-14.61	-14.91
8	wo	58.265	$9.67 \times 10^{38}$	N/A	-12.47	-13.32	-14.07	-14.51	-14.87
10	w	60.006	$9.26 \times 10^{38}$	5.0%	-11.15	-12.92	-14.17	-14.59	-14.89
10	wo	60.006	$9.26 \times 10^{38}$	5.0%	-12.15	-13.31	-14.15	-14.62	-14.98
14	w	64.410	$1.03 \times 10^{39}$	4.8%	-11.86	-13.40	-14.45	-14.92	-15.25
14	wo	64.410	$1.03 \times 10^{39}$	4.8%	-11.48	-13.35	-14.31	-14.83	-15.16
18	wo	68.730	$1.17 \times 10^{39}$	4.3%	-11.40	-13.30	-14.47	-15.04	-15.42
24	wo	74.269	$1.30 \times 10^{39}$	7.7%	-11.13	-13.07	-14.43	-15.09	-15.57
30	wo	80.787	$2.08 \times 10^{39}$	3.2%	-10.92	-12.93	-14.47	-15.23	-15.75
58	wo	108.510	$3.66 \times 10^{39}$	1.8%	-11.96	-13.57	-15.09	-15.78	-16.40
81	wo	131.245	$4.36 \times 10^{39}$	2.5%	-11.68	-13.69	-15.37	-16.08	-16.67

† w: model with nickel-mixing; wo: without nickel-mixing

Table 5.2: Observed Photometry

JD 2446800+	V	(B-V)	(U-B)	(V-R)	(V-I)
51.319	4.626	0.119	-0.749	0.224	0.279
52.322	4.516	0.228	-0.541		0.388
53.444	4.450	0.396	-0.261	0.344	0.448
54.394	4.434	0.507	0.235	0.384	0.491
58.297	4.445	0.966	1.325	0.441	0.656
60.271	4.401	1.145	1.548	0.459	0.718
64.255	4.285	1.361	1.824	0.505	0.816
68.251	4.221	1.458	1.986	0.565	0.950
74.249	4.105	1.559	2.116	0.657	1.049
81.246	3.966	1.594	2.237	0.700	1.092
109.232	3.178	1.615	2.608	0.643	1.051
130.295	2.96	1.57	2.51	0.69	1.04

(Menzies et al. 1987; Catchpole et al. 1987). No errors were listed.

Table 5.3: Moduli

JD	U	$\sigma_U^\dagger$	B	$\sigma_B$	V	$\sigma_V$	R	$\sigma_R$	I	$\sigma_I$
2446800+										
51.319	18.33	0.05	18.32	0.05	18.30	0.05	18.31	0.05	18.37	0.05
52.322	18.39	0.05	18.41	0.05	18.45	0.05	18.46	0.05	18.52	0.05
53.444	18.40	0.05	18.50	0.05	18.47	0.05	18.44	0.05	18.52	0.05
54.394	18.54	0.05	18.27	0.05	18.40	0.05	18.41	0.05	18.51	0.05
58.297	19.36	0.15	18.81	0.08	18.59	0.07	18.56	0.05	18.68	0.05
60.271	18.74	0.50	18.67	0.20	18.56	0.05	18.55	0.05	18.62	0.05
64.255	19.33	0.38	19.03	0.05	18.77	0.05	18.66	0.05	18.68	0.05
68.251	19.07	0.19	19.00	0.12	18.69	0.06	18.70	0.05	18.69	0.05
74.249	18.91	0.27	18.73	0.06	18.54	0.05	18.54	0.05	18.63	0.05
81.246	18.73	0.35	18.50	0.12	18.46	0.06	18.52	0.05	18.64	0.05
109.232	19.40	0.16	18.39	0.08	18.30	0.05	18.34	0.05	18.55	0.05
130.295	18.72	0.06	18.22	0.05	18.33	0.05	18.35	0.05	18.59	0.05

<sup>†</sup> Due to inherent uncertainties in photometry, a conservative minimum error of 0.05 has been assumed in all apparent magnitudes.

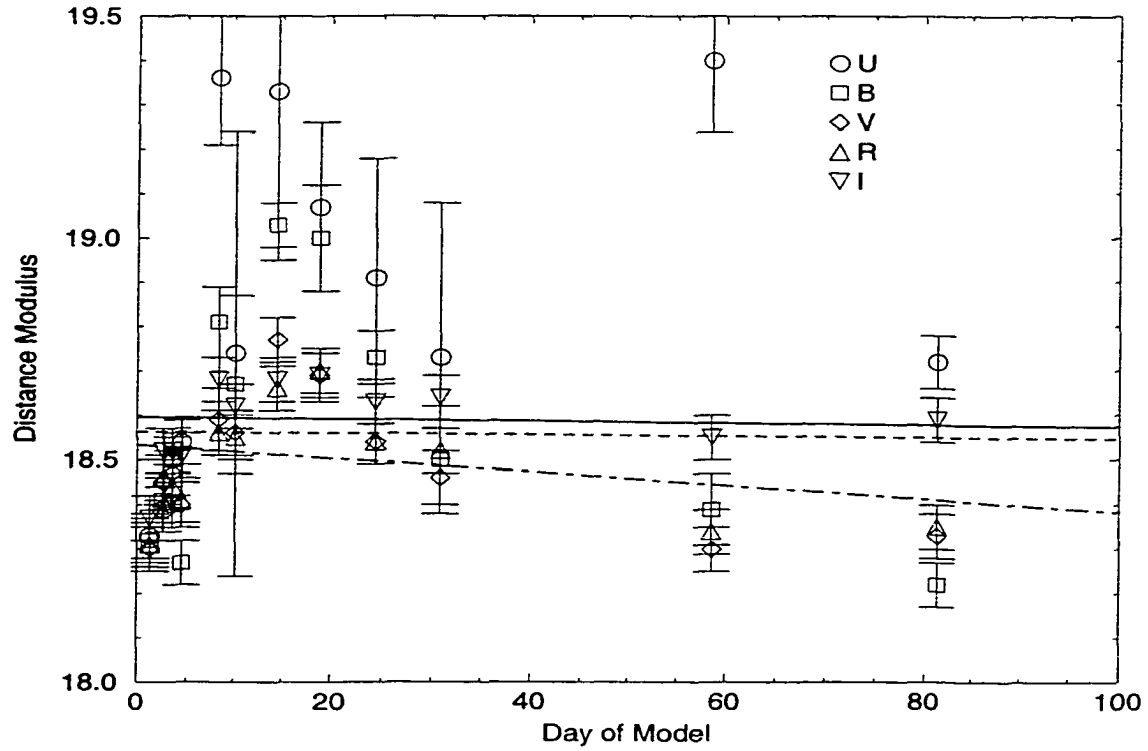


Figure 5.1: Color moduli derived for 1987A. Solid line: least-squares fit for all data. Dashed line: least-squares fit excluding Days 18 and 24. Dot-dashed line: least-squares fit excluding Days 18 and 24 and all UV data.

Table 5.4: Least-squares Fits of Color Moduli Graph

Line	mean $\mu$	$\sigma_{\mu}$	mags/day	$\sigma_{mags/day}$	d (kpc)	$\sigma_d$ (kpc)
Solid	18.59	0.26	-0.000223	0.00141	52.61	6.27
Dashed	18.56	0.26	-0.000158	0.00143	51.90	6.19
Dot-dashed	18.50	0.16	-0.00150	0.000983	50.26	3.70

Table 5.5: Other Distance Calculations

Distance (kpc)	Method	Source
$55 \pm 5$	EPM, $\xi = 1$	Branch (1987)
$43.3 \pm 4$	EPM	Chilukuri and Wagoner (1988)
$49 \pm 6$	EPM, $\xi < 1$	Eastman and Kirshner (1989)
$45.3 \pm 4$	EPM, $\xi < 1$	Schmutz et al. (1990)
$51.2 \pm 3.1$	ring (circular)	Panagia et al. (1991)
$< 46.77 \pm 0.76$	ring (circular)	Gould (1995)
$50.9 \pm 1.8$	ring (circular)	Panagia et al. (1997)
$48.6 \pm 2.2$	ring (circular)	Sonneborn et al. (1997)
$< 50.8 \pm 1.0$	ring (circular)	Gould and Uza (1998)
$48.8 \pm 1.1$	ring (elliptical)	Gould and Uza (1998)
$50 \pm 6$	ring (circular)	Garnavich et al. (1999)

## Chapter 6

# Conclusions

### 6.1 Results

Using the case of 1987A, PHOENIX has been able to test the validity of the hydrodynamic model of a supernova explosion and to identify what corrections are necessary to improve it. Beginning at Day 3, Blinnikov's 87A model failed to account for the strength of the Balmer lines in spite of the low photospheric temperature. Analysis of PHOENIX models led to the conclusion that additional  $^{56}\text{Ni}$  must be mixed into the ejecta in order that hydrogen atoms may be sufficiently excited by the resulting gamma radiation. The failure of the models to successfully reproduce the UV spectra of 87A when additional nickel is mixed lends further evidence that nickel-mixing must be negligible at higher velocities in the ejecta, where the UV spectrum is formed.

Photometry produced by Blinnikov's model deviates from observed photometry after Day 14, resulting in spectra that are too red through at least Day 81, but too blue by Day 103. By changing the luminosity parameter in his model, the temperature profile of a PHOENIX spectrum could be adjusted until it matched that of the observed spectrum. The new luminosity values give distance moduli for 87A that closely match

those predicted by the early-time spectra, giving further validity to this procedure.

The small uncertainty I obtained with my distance estimate ( $\leq 12\%$ ) is a substantial improvement over previous measurements using radiative, hydrodynamic, and thermodynamic models of 1987A. Only estimates using the circumstellar ring have yielded smaller uncertainties, but this method would be practical only for very close supernovae; the distances to further galaxies make direct observations of circumstellar rings highly unlikely.

## 6.2 Further Research

The failure of the 87A models to successfully reproduce the UV spectrum when extra nickel is mixed into the ejecta results from the fact that the current calculations only mixed nickel homogeneously. While more complicated nickel distributions allow the user more control, the parameter space becomes so large that finding a better fit would be very time consuming. Most theoretical models of supernovae call for velocity-limited nickel mixing and/or a steep power-law distribution. Future PHOENIX models that can simulate more refined hydrodynamical simulations are needed.

With the advent of new, more thorough detection programs, SN 1987A should not long remain the only supernova with sufficient detailed spectroscopic and photometric data to make it a candidate for PHOENIX's use. PHOENIX has the potential to be the most powerful tool available for testing hydrodynamic models of supernovae and for measuring their distances. A sufficiently large database of accurate supernova distances extending sufficiently far into the Hubble field would provide an independent means to determine an accurate value for the Hubble parameter and chart how it has varied over the history of the Universe, and ultimately how the expansion of the Universe will vary in the distant future.

# Bibliography

- W. D. Arnett, J. Bahcall, R. P. Kirshner, and S. E. Woosley. Supernova 1987A. *Ann. Rev. Astr. Ap.*, 27:629, 1989.
- E. Baron, P. H. Hauschildt, and T. R. Young. Supernova 1993J: One year later. *Physics Reports*, 256:23, 1995.
- S. Barthelmy et al. Supernova 1987A in the Large Magellanic Cloud. *IAU Circ. No. 4764*, 1989.
- R. M. Bionta et al. Observation of a neutrino burst in coincidence with supernova 1987a in the large magellanic cloud. *Phys. Rev. Lett.*, 58:1494, 1987.
- S. Blinnikov. Modeling of the light curve and parameters of the supernova 1987A. *Astronomy Letters*, 25:359, 1999.
- S. Blinnikov, P. Lundqvist, O. Bartunov, K. Nomoto, and K. Iwamoto. Radiation hydrodynamics of SN 1987A: I. global analysis of the light curve for the first 4 months. *ApJ*, 532:1132, 2000.
- David Branch. Blackbody emissivity of supernova 1987a and the extragalactic distance scale. *ApJ*, 320:L23, 1987.
- A. Burrows and K. A. Van Riper. A gamma-ray monte carlo study of the clumpy debris of SN 1987A. *ApJ*, 455:215, 1995.
- Jason A. Cardelli, Geoffrey C. Clayton, and John S. Mathis. The relationship between infrared, optical, and ultraviolet extinction. *ApJ*, 345:245, 1989.
- R. M. Catchpole et al. Spectroscopic and photometric observations of sn 1987a-II: Days 51 to 134. *MNRAS*, 229:15P, 1987.
- M. Chilukuri and R. V. Wagoner. Type II supernova photospheres and the distance to supernova 1987A. In Nomoto (1988), page 295.
- T. Dotani, K. Hayashida, H. Inoue, M. Itoh, K. Koyama, et al. Discovery of an unusual hard x-ray source in the region of supernova 1987A. *Nature*, 330:230, 1987.

- Ronald G. Eastman and Robert P. Kirshner. Model atmospheres for SN 1987A and the distance to the Large Magellanic Cloud. *ApJ*, 347:771, 1989.
- E. F. Erickson et al. Observation of Fe II (26.0 microns) in SN 1987A. *ApJ*, 330:L39, 1988.
- A. Fassia and W. P. S. Meikle.  $^{56}\text{Ni}$  dredge-up in supernova 1987A. *MNRAS*, 302:314, 1999.
- A. Fassia, W. P. S. Meikle, T. R. Geballe, N. A. Walton, D. L. Pollacco, R. G. M. Rutten, and C. Tinney.  $^{56}\text{Ni}$  dredge-up in the type IIp supernova 1995V. *MNRAS*, 299:150, 1998.
- B. Fryxell, E. Müller, and W. D. Arnett. Instabilities and clumping in SN 1987A. I - early evolution in two dimensions. *ApJ*, 367:619, 1991.
- P. Garnavich, R. Kirshner, and P. Challis. Supernova 1987A in the Large Magellanic Cloud. *IAU Circ. 7102*, page 1, 1999.
- Andrew Gould. The supernova ring revisited II. distance to the large magellanic cloud. *ApJ*, 452:189, 1995.
- Andrew Gould and Osamu Uza. Upper limit to the distance to the large magellanic cloud. *ApJ*, 494:118, 1998.
- P. H. Hauschildt and E. Baron. Numerical solution of the expanding stellar atmosphere problem. *J. Comp. Applied Math.*, 109:41, 1999.
- P. H. Hauschildt and L. Ensmann. Analysis of the early spectra and light curve of SN 1987A. *ApJ*, 424:905, 1994.
- M. Herant and W. Benz. Hydrodynamical instabilities and mixing in SN 1987A - two-dimensional simulations of the first 3 months. *ApJ*, 370:L81, 1991.
- M. Herant and W. Benz. Postexplosion hydrodynamics of SN 1987A. *ApJ*, 387:294, 1992.
- M. Herant, W. Benz, W. R. Hix, C. L. Fryer, and S. A. Colgate. Inside the supernova: A powerful convective engine. *ApJ*, 435:339, 1994.
- K. Hirata et al. Observation of a neutrino burst from the supernova SN1987A. *Phys. Rev. Lett.*, 58:1490, 1987.
- P. Höflich. IAU Colloquium 108: Atmospheric diagnostics of stellar evolution. In Nomoto (1988), page 288.
- J. P. Hughes, C. E. Rakowski, D. N. Burrows, and P. O. Slane. Nucleosynthesis and mixing in Cassiopeia A. *ApJ*, 528:L109, January 2000.

- K. Kifonidis, E. Müller, and T. Plewa. Non-spherical core collapse supernovae and nucleosynthesis. *Nucl. Phys. A*, in press.
- K. Kifonidis, T. Plewa, H.-Th. Janka, and E. Müller. Nucleosynthesis and clump formation in a core-collapse supernova. *ApJ*, 531:L123, 2000.
- Cecilia Kozma and Claes Fransson. Late spectral evolution of SN 1987A: I. temperature and ionization. *ApJ*, 497:431, 1998a.
- Cecilia Kozma and Claes Fransson. Late spectral evolution of SN 1987A: II. line emission. *ApJ*, 496:946, 1998b.
- H. Li, R. McCray, and R. A. Sunyaev. Iron, cobalt, and nickel in SN 1987A. *ApJ*, 419:824, 1993.
- Peter Lundqvist and Claes Fransson. The line emission from the circumstellar gas around SN 1987A. *ApJ*, 464:924, 1996.
- S. M. Matz, G. H. Share, M. D. Leising, E. L. Chupp, W. T. Vestrand, et al. Gamma-ray line emission from SN1987A. *Nature*, 331:416, 1988.
- R. McCray. Supernova 1987A revisited. *Ann. Rev. Astr. Ap.*, 31:175, 1993.
- J. W. Menzies et al. Spectroscopic and photometric observations of sn 1987a: the first 50 days. *MNRAS*, 227:39P, 1987.
- K. Nomoto, editor. *IAU Colloquium 108: Atmospheric Diagnostics of Stellar Evolution*, Berlin, 1988. Springer.
- N. Panagia, R. Gilmozzi, R. P. Kirshner, C. S. J. Pun, G. Sonneborn, and SINS Collaboration. Improved distance determination to SN 1987A and the LMC. *Bull. Amer. Astr. Soc.*, 29:1243, 1997.
- N. Panagia, R. Gilmozzi, F. Macchetto, H.-M. Adorf, and R. P. Kirshner. Properties of the SN 1987A circumstellar ring and the distance to the Large Magellanic Cloud. *ApJ*, 380:L23, 1991.
- M. Phillips, M. Hamuy, S. Heathcote, N. Suntzeff, and S. Kirhakos. An optical spectrophotometric atlas of supernova 1987A in the LMC. I - the first 130 days. *AJ*, 95:1087, 1988.
- C. S. J. Pun et al. Ultraviolet observations of SN 1987A with the IUE satellite. *ApJ Suppl.*, 99:223, 1995.
- A. Riess et al. The farthest known supernova: Support for an accelerating universe and a glimpse of the epoch of deceleration. *ApJ*, page in press, 2001.

- W. Schmutz, D. C. Abbott, R. S. Russell, W.-R. Hamann, and U. Wessolowski. Non-LTE model calculations for SN 1987A and the extragalactic distance scale. *ApJ*, 355:255, 1990.
- C. I. Short, P. H. Hauschildt, and E. Baron. Massive multi-species, multi-level, NLTE atmosphere models of novae in outburst. *ApJ*, 525:375, 1999.
- G. Sonneborn, C. Fransson, P. Lundqvist, A. Cassatella, R. Gilmozzi, R. P. Kirshner, N. Panagia, and W. Wamsteker. The evolution of ultraviolet emission lines from circumstellar material surrounding SN 1987A. *ApJ*, 477:848, 1997.
- Y. Takeda. Formation of H and He lines and atmospheric diagnostics in type II supernovae. *A&A*, 245:182, 1991.
- V. P. Utrobin, N. N. Chugai, and A. A. Andronova. Asymmetry of SN 1987A: Fast ni-56 clump. *A&A*, 295:129, March 1995.
- F. C. Witteborn, J. D. Bregman, D. H. Wooden, P. A. Pinto, D. M. Rank, et al. Spectral line profiles of nickel and argon in supernova 1987A - expansion velocity and electron scattering effects. *ApJ*, 338:L9, 1989.
- S. E. Woosley. SN 1987A - after the peak. *ApJ*, 330:218, 1988.

## Chapter 7

# Appendix

### 7.1 REZONE

REZONE is a program developed during the course of this research project to improve the resolution of the model supernova envelope between PHOENIX iterations. The full code is too long to reproduce here.

The model supernova envelope employed by PHOENIX consists of a grid of 100 zones in velocity-space, the boundaries of which are preset by the user. During the course of the PHOENIX iterations, the values of the temperatures, densities, opacities, and pressures are converged upon for each zone. Oftentimes, after several iterations one notes large jumps in the parameter values from one zone to the next, most notably when the model develops a very thin photosphere. PHOENIX has difficulty converging when there are large discontinuities in temperature and opacity, so it becomes necessary to increase the number of zones in the vicinity of the photosphere. This is performed at the expense of removing zone boundaries from other parts of the model where lower resolution can be allowed, most often at the top of the envelope where the temperature and opacity profiles are much shallower. This is necessary as PHOENIX is designed to read a fixed

number of zones.

REZONE uses several subroutines and modules employed by PHOENIX. The program first reads the model to be rezoned using the PHOENIX readfile subroutine, and stores the parameter values in PHOENIX data modules. REZONE then scans the data modules for those parameters corresponding to the velocity value that is to be removed, and for the location in velocity-space where the new zone boundary is to be inserted.

To assign parameters for the new zone boundary, the program calls the Fortran subroutine `polint` to calculate approximate values using the two existing zone boundaries surrounding the new boundary and assuming a constant slope for the parameter curve between the existing zones. Parameter values are subsequently shifted to remove the discarded zone and insert the new one, and the PHOENIX writefile subroutine is used to write the new, rezoned model.  $b_i$  values, which are independent of the zone structure, are simply copied from the original model to the rezoned model.

For a 100-zone velocity-space model with a difference of  $100 \text{ km s}^{-1}$  or less between consecutive zones, a constant slope in the density profile between zones may be considered a good approximation. Tests were performed to measure the total mass of the model supernova envelope after ten rezonings, a number usually more than sufficient to correct all discontinuities. In all cases, the result agreed with the total mass before rezoning to within 0.1%. Temperature, pressure, and opacity values are treated only as first guesses at the start of each iteration and are recalculated by PHOENIX, therefore assuming a constant slope is of no concern. Radius is assumed to be determined by the equation  $r = vt$ , and so a constant slope would be exact.